AN EXPERIMENTAL AND THEORETICAL INVESTIGATION

OF A FINITE BETA MODIFIED DRIFT WAVE

Thesis by

Eric Fredrickson

In Partial Fulfillment of the Requirements

for the Degree of

Doctor of Philosophy

California Institute of Technology

Pasadena, California

1985

(Submitted July 30, 1984)

ACKNOWLEDGEMENTS

I would like to thank my advisor, Paul Bellan, for his support over the years of this research. I am also especially grateful to Paulett Liewer and Stewart Zweben for their considerable help and support, without which this work would not have been done. I would like to thank Glenn Greene for much helpful advice and Frank Cosso for his help with the equipment used in these experiments. This work was supported in part by DOE contract #DE-FG03-84ER53173.

ABSTRACT

The saturated state of a low frequency, coherent, m=2, global mode has been studied in the Encore tokamak using probe techniques. The mode is found to have large fluctuations in density, electron temperature, space potential and magnetic field. The equilibrium plasma characteristics were also determined with probe measurements. Magnetic probes were used to determine the radial profile of the poloidal magnetic field, from which the rotational transform and current density profiles could be deduced. A Langmuir probe was used to measure radial profiles of the density, electron temperature and space potential.

By comparing the experimental measurements with the predictions of a computer code, the mode was identified as a finite β_T modified drift wave. The code is based on a linear, two-fluid theory of the coupling of drift and shear-Alfven modes. Of the two shear-Alfven solutions and the drift branch solution, it was found that the drift wave solution best fit the observed frequency of the mode and the relative amplitudes of the density, space potential and magnetic fluctuations. The identification of the mode as a finite β_T modified drift wave means that the mode is more closely related to the higher frequency, turbulent fluctuations observed on larger machines, rather than the lower frequency, coherent Mirnov oscillations.

TABLE OF CONTENTS

I INTRODUCTION

Anomalous energy transport has been a serious problem for magnetic confinement devices since the inception of the controlled fusion program in the 50's. Anomalous, in this sense, means that the losses are larger than can be explained by collisional and atomic process alone. One of the likely causes of the anomalous transport is the magnetic and density fluctuations observed on virtually all magnetic confinement devices[1]. In tokamaks, these fluctuations can be classified into two general types, low frequency, long wavelength coherent modes (often called Mirnov oscillations) and higher frequency, shorter wavelength, strongly turbulent fluctuations. The Mirnov oscillations are generally considered to be primarily magnetic perturbations and can be treated with the resistive magnetohydrodynamic equations[2]. The turbulence is in the drift range of frequencies, and non-linear saturated states of drift or drift-Alfven waves are considered to be strong candidates for an explanation of these fluctuations. Even a low level of magnetic or electrostatic turbulence can result in a large increase in radial transport and, as a result, much work has been devoted towards understanding drift and drift-Alfven waves.

In this thesis, strong coherent fluctuations in density and magnetic field, observed in the Encore tokamak, have been studied experimentally and theoretically. Probe measurements show that the mode has large fluctuations in density, electron temperature, space potential and magnetic field. The poloidal and toroidal mode numbers, as well as the radial structure of the fluctuations have been measured. Modes with toroidal mode numbers n=1 and poloidal mode numbers m=1,2 and 3 have been identified. The equilibrium plasma characteristics were also determined with probe measurements. Magnetic probes were used to determine the radial profile of the poloidal magnetic field, from which the

rotational transform and current density profiles could be deduced. A Langmuir probe was used to measure radial profiles of the density, electron temperature and space potential.

This thesis will deal primarily with the identification of the experimentally observed m=2 mode. Questions concerning the theoretical stability of the mode and the transport associated with it will not be directly addressed. To help identify the mode a numerical code was developed to solve a linearized set of the two-fluid equations, simplified by the assumption of low frequency, $\omega \ll \omega_{ci}$, and other assumptions consistent with the experimental parameters. The code solves the resulting reduced set of equations in bounded cylindrical geometry. A similar set of equations has been used by previous authors to investigate the short wavelength drift-Alfven modes[3-6].

In a warm magnetized plasma these equations have two types of solutions, the ion-acoustic waves and the shear-Alfven waves. In the presence of a density gradient perpendicular to the magnetic field, the ion-acoustic wave is modified to become the drift wave, which is basically electrostatic and propagates nearly perpendicular to the magnetic field[7]. The shear-Alfven waves are electromagnetic waves in which the ion mass provides the inertial force and the resistance of the magnetic field lines to bending provides the restoring force[8]. They propagate nearly parallel to the magnetic field at approximately the Alfven velocity, $v_A \equiv B(4\pi n m_i)^{-\frac{1}{2}}$. When the parallel phase velocity of the drift wave approaches v_A, the drift and Alfven branches become coupled and the drift wave acquires a strong magnetic component.

Of the two shear-Alfven solutions and the drift branch solution, it was found that the drift wave solution best fit the observed frequency of the mode and the relative amplitudes of the density, space potential and magnetic fluctuations. The shear-Alfven solutions had much larger magnetic fluctuations for a given

level of density fluctuations. The identification of the mode as a finite β_T, ($\equiv 8\pi nT/B^2$), modified drift wave means that the mode is more closely related to the higher frequency, turbulent fluctuations observed on larger machines, rather than the lower frequency coherent Mirnov oscillations.

Previously, similar modes with large, well correlated density and magnetic fluctuations have been observed on linear arcjet plasma devices at Nagoya[9] and at UCLA[10]. These machines also operate at parameters similar to those in Encore. They are physically smaller, and observations on the modes were limited to comparison of the observed scaling of frequencies and amplitudes of the fluctuating quantities to the predictions of a local theory.

In Chap. II the machine and diagnostics will be described and the results of the experimental measurements presented. In Chap. III the linear equations describing the coupling of the drift and Alfven branches will be derived and a simplified version will be solved analytically. Numerical solution of the equations will be discussed and the results of the calculations will be presented. In Chap. IV the results will be discussed and some conclusions presented. Details of the numerical calculations, the theory of probes and their construction and other observations can be found in the Appendices.

II EXPERIMENT

A Description of the Encore Tokamak

The experiments were performed on the Caltech Encore tokamak. The principal features of this machine are the high pulse repetition rate, typically 15 shots per second, and the fact that the plasma is cold enough so that probes can be inserted as far as the center of the discharge. The high repetition rate is achieved by using a steady state toroidal field (variable from 0.1 to 1.5 kG) and a high power audio-frequency amplifier as the ohmic heating power supply. The maximum plasma current is limited to about 10 kA by the power available from the OH amplifier, but in practice, the requirement that the probes survive the heat load from the plasma limits the plasma current to less than about 4 kA. Typical densities and electron temperatures were $n \approx 10^{12}$ cm^{-3} and $T \approx 10-15$ eV. The length of the discharges was $\approx$4 ms, variable from 3-6 ms.

The 1.27 cm thick aluminum vacuum chamber walls provide some stabilization for the plasma; a pulsed vertical field makes up for flux lost in the resistive decay of the wall currents. Access to the plasma is provided by 33 small (4 cm diameter) and 15 large (8 x 22 cm) ports. The plasma minor radius is 12.6 cm, with the wall acting as a limiter. The major radius is 38.1 cm, resulting in an aspect ratio of three.

The plasma energy loss is dominated by line radiation from the neutral or partially stripped gas. Estimates of the radiated power based on the calculations of Post et al.[11] show that radiation can acount for nearly all of the input ohmic heating power. In the highest current hydrogen discharges the plasma does burn through this radiation dominated regime, but the discharges were not sufficiently reproducible for making shot-to-shot measurements, and were also hot enough to destroy any probes exposed for short periods of time to the

plasma. For these reasons, it was not practical to do experiments in burn-through discharges. Argon, being easier to ionize, gave more reproducible discharges and was typically used as the filling gas. Argon plasmas also did not have the high levels of X-ray radiation encountered in hydrogen discharges. Discharges run with hydrogen, helium and nitrogen were similar to the argon discharges, but were less reproducible.

The practical limits on plasma current, and hence density and temperature, were set by the requirements that the plasma break down reproducibly and that the probes could withstand the heat flux resulting from the high duty cycle (~8%). The acceptable range of plasma currents was then about 1.5 to 4.0 kA, the lower limit was set by the requirement of consistent breakdown, and the upper limit by the maximum tolerable heat flux to the probes. For most of the data presented in this work, a q at the wall of between three and four was desirable, where $q(r)$ for a cylindrical tokamak is defined as[12]

$$q(r) \equiv \frac{\partial \Psi_{tor}}{\partial \Psi_{pol}} \approx \frac{r\, B_T}{R\, B_\theta(r)} , \tag{2.1}$$

here r is the minor radius, R is the major radius, B_T is the toroidal field and B_θ is the poloidal field (as shown in Fig. 1.) Thus, the typical toroidal field strengths were between 200 and 500 gauss. These parameters lead to a plasma β_T, defined as the ratio of plasma pressure to magnetic field pressure, of $\beta_T \equiv 8\pi nT/B^2 \approx .01-.02$. Within this range of parameters, it was possible to obtain reproducible discharges relatively insensitive to the presence of probes.

The principal plasma diagnostics were two moveable Langmuir probes and three moveable magnetic probes (see Figs. 1 and 2). The magnetic probes consisted of small, air cooled coils, oriented so that the time integrated signal gave the local poloidal magnetic field strength. The construction and calibration of these probes is described in more detail in Appendix B. The probes were

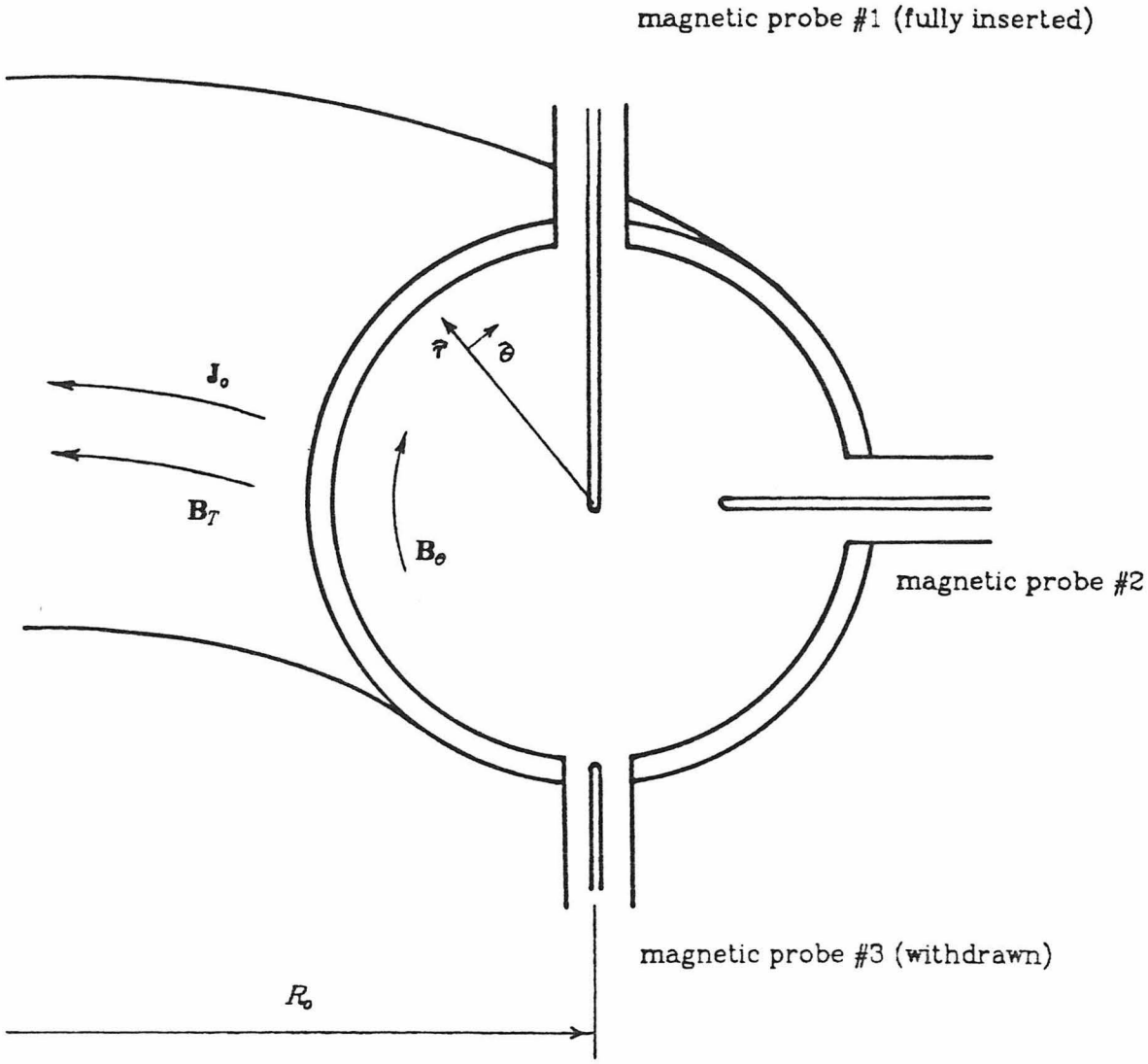

Figure 1. This figure shows the orientation of the three magnetic probes described in Chap. 2. Also shown are the orientation of the toroidal field, plasma current and poloidal field.

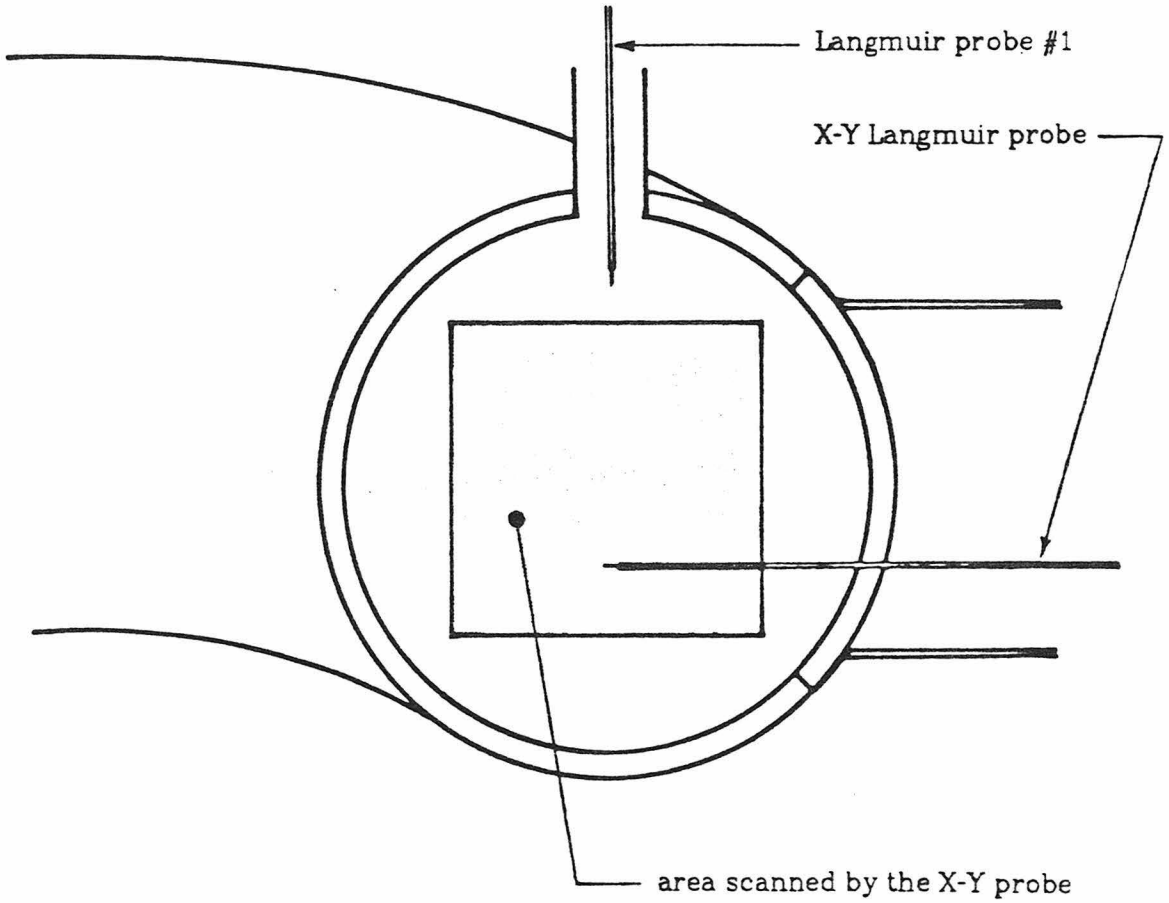

Figure 2. This figure shows the orientation of the two Langmuir probes described in Chapter 2. The shaded region shows the region of travel of the X-Y probe.

mounted on stepper motor driven probe drives, controlled by an LSI-11/23 computer. One probe drive (the X-Y drive) could scan a probe over most of the plasma minor cross-section (see Fig. 2). The other probe drives (the linear drives) moved the probes only in the radial direction. The magnetic probes and one Langmuir probe were mounted on the linear probe drives and a second Langmuir probe was mounted on the X-Y probe drive.

B Measurement of the Equilibrium Profiles

Oscilloscope traces of the plasma current, loop voltage and probe signals are presented in Fig. 3. and a typical set of data showing the equilibrium safety factor, density, electron temperature and space potential profiles is presented in Fig. 4. The data presented in these figures were collected over a period of about 30 minutes of machine running time, corresponding to ≈30,000 shots. Data points were collected in only a small fraction of these shots, <5,000; most of the time was spent in moving the probes and in transfering, processing and making permanent records of the data. The plasma was highly reproducible; variations in global quantities such as plasma current, loop voltage, and density were typically less than a few percent over the 30,000 shots. As can be seen, the profiles are often not smooth, but for a given set of discharges in a run, these profiles were reproducible.

The density, space potential and electron temperature (solid curve) were measured with the Langmuir probe. The electron temperature profile with the dashed line was computed from the plasma current density profile, assuming Spitzer resistivity[13,14] and using $Z_{eff} = 4.5$, (Z_{eff} is the average charge state of the ions), i.e.,

$$T_e = 5.3 \left[\frac{Z_{eff}\, J(r)}{V_{loop}} \right]^{\frac{2}{3}} , \qquad (2.2)$$

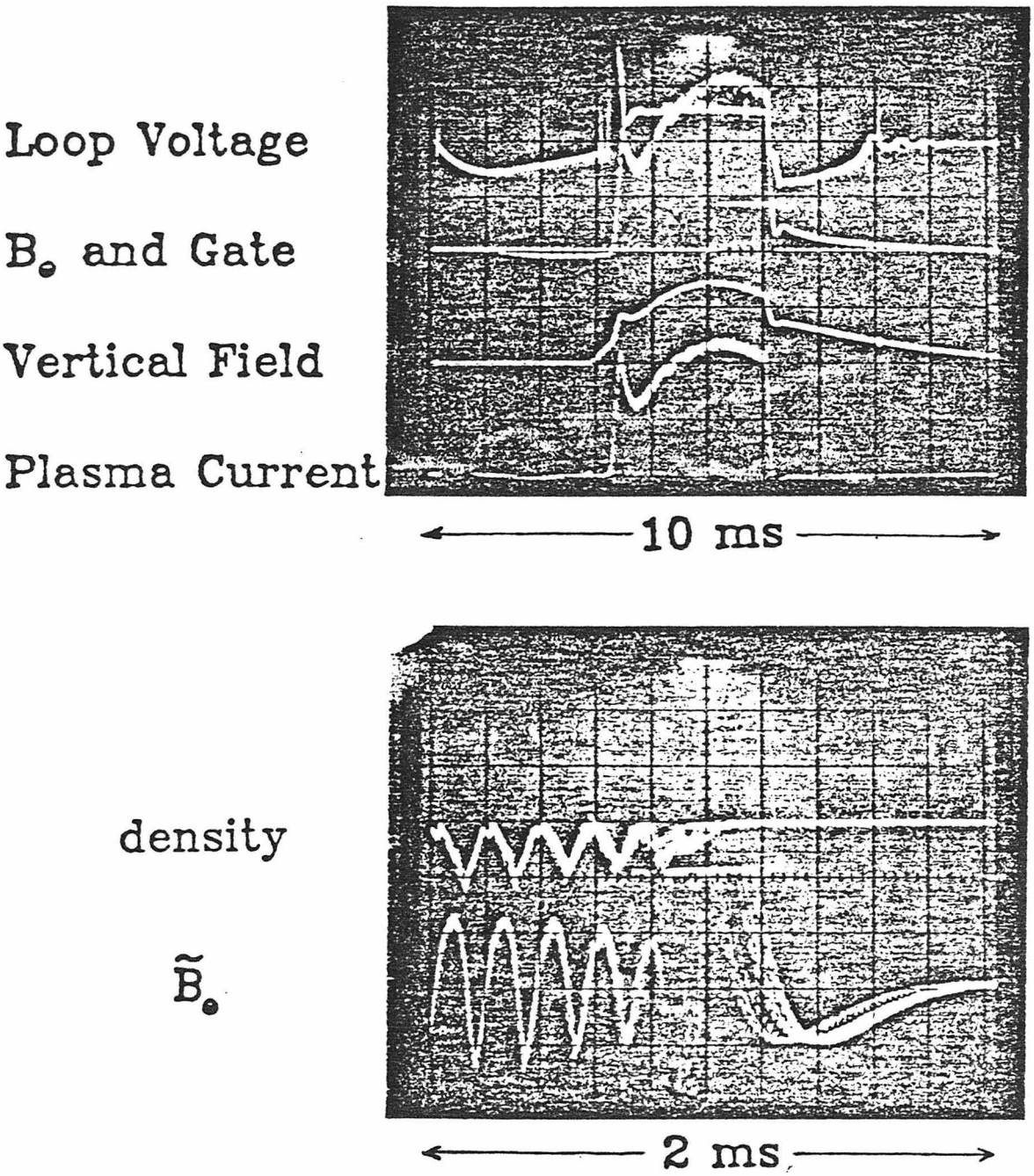

Figure 3. The upper oscilloscope photograph shows the typical loop voltage (10 volts/div), poloidal magnetic field at the wall (as measured with a magnetic probe), vertical field current (16 A/div) and plasma current (2 kA/div). The time axis is 1 ms/div or 10 ms full scale. The lower photograph shows the density and magnetic fluctuations on an expanded scale, .2 ms/div or 2 ms full scale.

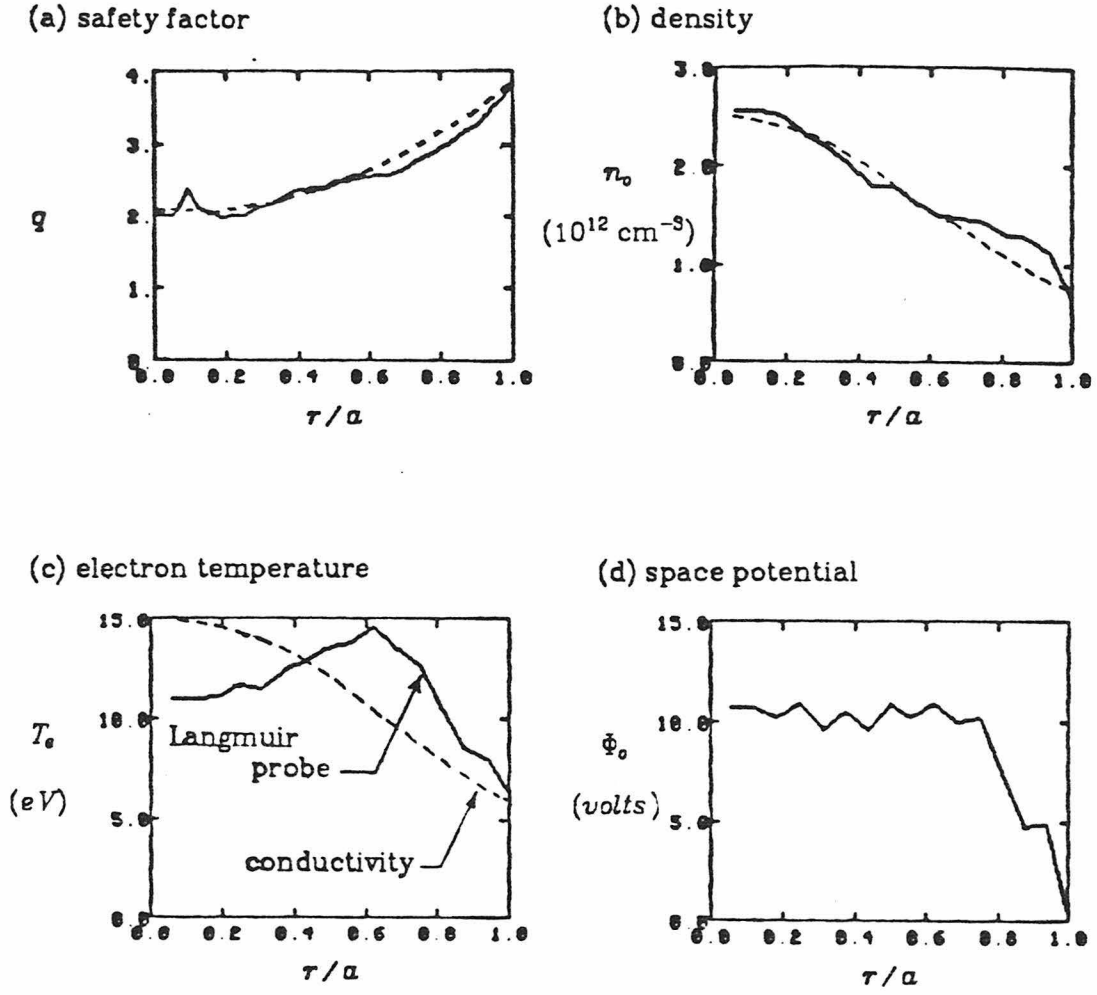

Figure 4. Radial profiles of the (a) safety factor, $q(r)$, (b) density, (c) electron temperature and (d) space potential. The broken lines in Figs. 4(a), 4(b) and 4(c) are the profiles used in the numerical code when computing the results presented in Fig. 11. The flatness of the space potential in the central regions indicates a very small radial electric field, and thus it is not necessary to include a doppler shift to the measured frequency due to **E**×**B** drift. The toroidal field for these data was 350 gauss.

where T_e is in eV and $J(r)$ is in A/cm^2; $J(r)$ is computed from the measured B_θ profile. The choice of Z_{eff} = 3–6 is based on a comparison of the plasma conductivity and the Langmuir probe measurement of the electron temperature and is found to be consistent with the predictions of Post et al.[11]. The two measurements are in rough agreement, but the shape of the profiles is different. The error in the conductivity measurement was probably less than 10%, and the error in the Langmuir probe temperature was less than 5%, so these measurements would indicate that the Z_{eff} of the plasma was a function of the minor radius.

The density, temperature and space potential were determined from measurements of the ion saturation current and a sixteen point I-V characteristic for Langmuir probe 1 in Fig. 2. The sixteen bias voltages for the I-V characteristic were chosen so that the temperature of the bulk electrons (i.e., not the tail of the distribution function), would be measured. The temperature was calculated from the data by a least squares fit to the theoretical Langmuir probe characteristic. This fit also predicted the plasma space potential. A more detailed discussion of this analysis is presented in Appendix B. The density was then determined from the ion saturation current from:

$$I_{sat} = nec_s A \ , \tag{2.3}$$

where n is the local electron density, $c_s = (T_e/m_i)^{\frac{1}{2}}$ and A is the area of the probe. The Langmuir probe measurements of density were compared to the line averaged density of the plasma measured by a 3mm microwave interferometer and were found to be in good agreement.

As measurement of the absolute space potential in a magnetized plasma with a Langmuir probe is difficult, the common practice is to relate fluctuations in the floating potential with space potential fluctuations. The presence of

strong fluctuations in the electron temperature meant that this practice was not valid, and thus necessitated this direct measurement of the space potential.

The magnetic probes were used to measure the time dependent poloidal magnetic field. Because the amplitude of the magnetic fluctuations was $\leq 5\%$ of the 'dc' poloidal field, the fluctuating field component was amplified and digitized independently of the total poloidal field. The total poloidal field was then averaged over time to give the dc poloidal field component. This time averaged magnetic field data could be used to calculate an approximate safety factor profile, $q(r)$. When $q(r)$ is equal to a rational number, m/n, the magnetic field structure will be resonant with a mode having poloidal mode number m and toroidal mode number n (i.e., $\mathbf{k}\cdot\mathbf{B} = 0$, where $\mathbf{k} \equiv \frac{m}{r}\hat{\theta} + \frac{n}{R}\hat{\varphi}$). Near the mode rational surface, the mode wavelength along the magnetic field becomes very long and the electron response becomes dominated by collisions; the stability and structure of low m modes is strongly affected by the presence of these mode rational surfaces.

In principle, it is necessary to know the complete toroidal and poloidal structure of the magnetic fields to calculate $q(r)$. In practice, it is a good approximation to neglect any toroidal dependence in the time averaged fields, and then make some assumption about the poloidal dependence of the poloidal magnetic field. The simplest assumption is that the flux surfaces are circular and concentric, which is equivalent to the assumption that $\beta_T \ll 1$ and the aspect ratio, R/a, is large[15], (R and a are, respectively, the major and minor radii of the vacuum vessel). With these assumptions, the expression for the safety factor in terms of the poloidal magnetic field measured from the top or bottom, (probes 1 and 3 in Fig. 1), of the machine is:

$$q(r) = \frac{r\,B_T}{R\,B_\theta(r)}\left(1-(r/R)^2\right)^{-\frac{1}{2}}\,, \tag{2.4}$$

For measurements made at other poloidal angles, the expression for $q(r)$ is slightly different, but in general, near $r = 0$, $q(r)$ is very nearly the same as for the straight cylinder case.

C Measurement of the Mode Structure

Strong, coherent fluctuations in density and magnetic field were observed over a wide range of plasma parameters. The discharges in which these waves were seen can be divided into three categories: those with $q(0) \approx 1$, those with $q(0) \approx 2$ and those with $q(0) > 2$. This work will deal primarily with discharges in the second category, $q(0) \approx 2$. In the discharges with $q(0) \approx 1$, it was observed that the density fluctuations had a dominant poloidal mode number of one, but that the magnetic fluctuations were dominantly $m = 2$. The coupling of different poloidal modes by toroidal geometry is of considerable interest, but the equations involved are more complex than those for a single poloidal mode. For this reason, although many experimental measurements were made (cf. Appendix C), no theoretical calculations will be discussed describing these discharges. In discharges with $q(0) > 2$, the experimental measurements were harder to interpret as there was strong evidence that more than one poloidal mode was present and the modes tended to be localized more to the periphery of the plasma (where it was difficult to make good measurements). Thus, the discharges with $q(0) \approx 2$ offered the greatest possibility for successful comparison of theory to experiment.

A typical data set showing the mode structure for discharges with $q(0) \approx 2$ is presented in Figs. 5-9 at the end of this chapter. In these discharges a coherent mode (or wave) was observed with a frequency of $\sim$ 2 - 5 kHz. These modes had a poloidal mode number of $m = 2$ and a toroidal mode number of $n = 1$. The q at the center of the plasma was approximately two. Within the

errors in calibration it was not possible to determine whether or not a mode rational surface actually existed in the plasma; if it did it was very near the plasma center.

The time dependence of the fluctuating quantities was measured by digitizing the signal over a time somewhat longer than the period of the mode oscillations. The Langmuir probe measurements were digitized over a period of typically 512 μs, with 16 samples at 32 μs intervals. The magnetic fluctuations were digitized with a different instrument, the data collection interval was 640 μs, with 32 samples at 20 μs intervals. Each data point was additionally averaged over four shots, and the spatial structure of the mode was determined by moving the probe to different spatial locations between shots. The Langmuir probe characteristic required measurements for sixteen different probe bias voltages as well as measurement of the ion saturation current and the floating potential. A set of data was then necessarily collected over many plasma shots. To maintain a constant phase reference, a separate Langmuir probe signal was used as a reference to trigger the data collection system.

Contour plots of the density, temperature, space potential and parallel component of the vector potential are presented in Fig. 5. What appears as the poloidal angle in the plots is the time history of the mode measured at the fixed poloidal angle of the probe. As the mode is rotating, time can be mapped into poloidal angle, but the object here was just to present the data in a form as close to that of the real mode structure as possible. As the parameters of the discharge and the amplitude of the mode are changing, the contours do not exactly match at $\theta = 0, 2\pi$.

The magnetic structure of the mode was investigated with three moveable magnetic probes located on the top, outside and bottom of the machine. Each probe was moved along a minor radius from the center of the vacuum chamber

to the wall. The time dependent behavior of the magnetic field was measured at 32 radial positions. From the relative phase shifts in the fluctuating components of the magnetic field between the three probes it was possible to determine the dominant poloidal mode number of the magnetic fluctuations to within an additive factor of four. (The factor of four results from the minimum poloidal spacing of 90° for the probes.) For the discharges with $q(0) \approx 2$, the dominant poloidal mode structure was $m = 2$. The fluctuating magnetic field was spatially integrated from the center of the plasma to find the radial structure of the vector potential using the relation

$$\tilde{B}_\theta = (\nabla \times \mathbf{A})_\theta \approx -\frac{\partial \tilde{A}_\parallel}{\partial r} \quad , \tag{2.5}$$

In this expression, the components of the vector potential perpendicular to the magnetic field have been ignored (thus ignoring coupling to the compressional Alfven waves). This approximation is valid in the limit of low β_T discharges[16] (here $\beta_T \approx .01-.02 \ll 1$).

To investigate the electrostatic structure of the mode, two Langmuir probes were used. The first of these scanned a large part of the plasma minor cross-section to determine the dominant poloidal mode number of the electrostatic fluctuations. Measurements were made of both the ion saturation current fluctuations and the floating potential fluctuations. The dominant poloidal mode structure of these was the same, that is, $m = 2$ for the discharges with $q_o \approx 2$. Since measurement of the floating potential was less perturbing to the plasma and less damaging to the probe, most of the subsequent measurements were made of the floating potential. By making measurements of the floating potential contours at several closely spaced times during the shot, it was possible to determine the direction of the mode propagation. In Fig. 6 a set of these data is presented in which the rotation can be seen to be in the electron

diamagnetic drift direction (arrow).

The radial profiles of the amplitudes of the density, electron temperature, vector potential and space potential fluctuations, as well as the phase relative to a fixed reference, is presented in Figs. 7 and 8. The ratio of the inductive to electrostatic components of the parallel electric field are presented in Fig. 9; for the experimental data (the filled circles in the figure) the maximum value of the ratio is ≈ 0.1. The level of density fluctuations was very large, $\tilde{n}/n \approx 0.4$ at $r/a = 0.6$. The amplitude of the vector potential fluctuations was found to be approximately 1.5 statvolts, corresponding to a fluctuation in B_θ of 0.5 - 1.0 gauss. The density fluctuations led the magnetic fluctuations by approximately 90°. The temperature fluctuations were out of phase by 180° with the density fluctuations. This would be expected for a radiation dominated discharge as the radiated power scales as n^2. The temperature fluctuation level was also large, with $\tilde{T}/T \approx 0.13$ at $r/a = 0.6$. This temperature fluctuation level is large enough to affect the local plasma resistivity, and therefore would be important in a theory describing the coupling of electrostatic to magnetic fluctuations. The space potential fluctuations were found to lead the density fluctuations by $\approx 45°$; thus the **E×B** drift would transport plasma inwards, and in the simple theory would be associated with damping of the mode[17]. The amplitude of the space potential fluctuations is approximately 2.5 volts at $r/a = 0.6$, corresponding to $e\tilde{\Phi}/T \approx 0.18$.

The measurements presented above are typical for all the $q(0) \approx 2$ discharges studied. The absolute level of the fluctuations was observed to vary somewhat, and in some cases the relative phases were not as cleanly defined as in this set of data. The toroidal field was varied over a range from $\approx$ 200 to 400 gauss in an attempt to determine the scaling of the frequency or mode amplitudes on B_T. The results were inconclusive; the frequency was found to vary, but

not in a consistent fashion. Later numerical work also showed that the frequency was a weak function of toroidal field in this parameter range, but could depend strongly on other, less controllable plasma parameters. Likewise, no consistent scaling with B_T of the relative mode amplitudes was observed.

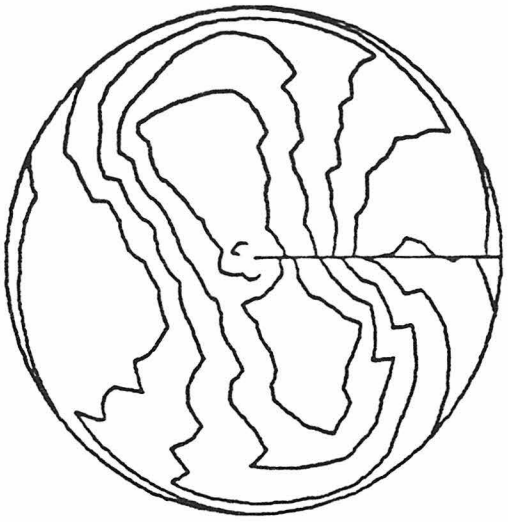

(a) Density ($0.5 \cdot 10^{12}$/ contour)

(b) Electron temperature (2.5 eV/contour)

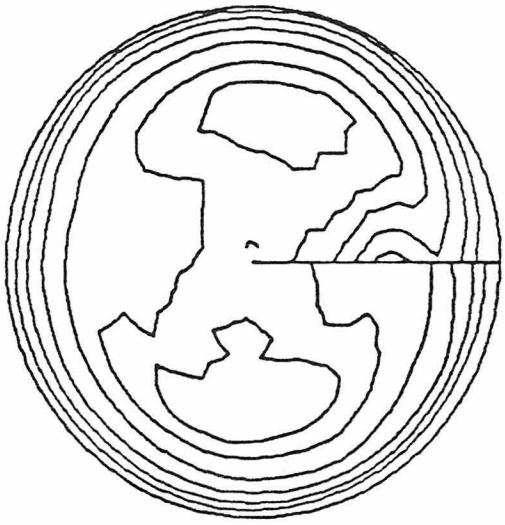

(c) Space potential (2.5 volts/contour)

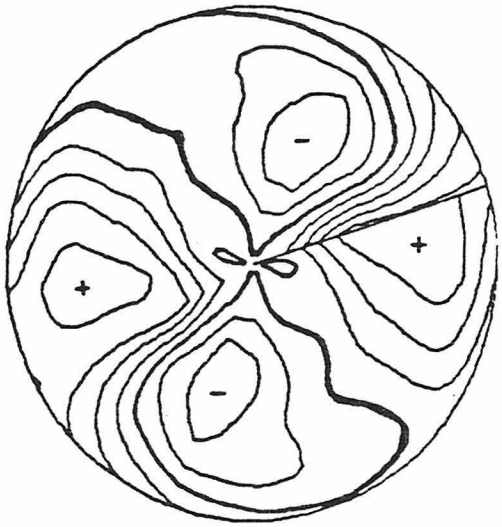

(d) Vector potential (1 statvolt/contour)

Figure 5. Contour plots of the (a) density, (b) electron temperature, (c) space potential and (d) vector potential. The figures are plotted such that the poloidal angle corresponds to the time axis, scaled so that 2π radians corresponds to twice the wave period. The contour plots then approximate the actual spatial structure of the modes. The solid line corresponds to $t = 0$. The contours do not actually match at this point as the plasma characteristics and mode structure are slowly changing.

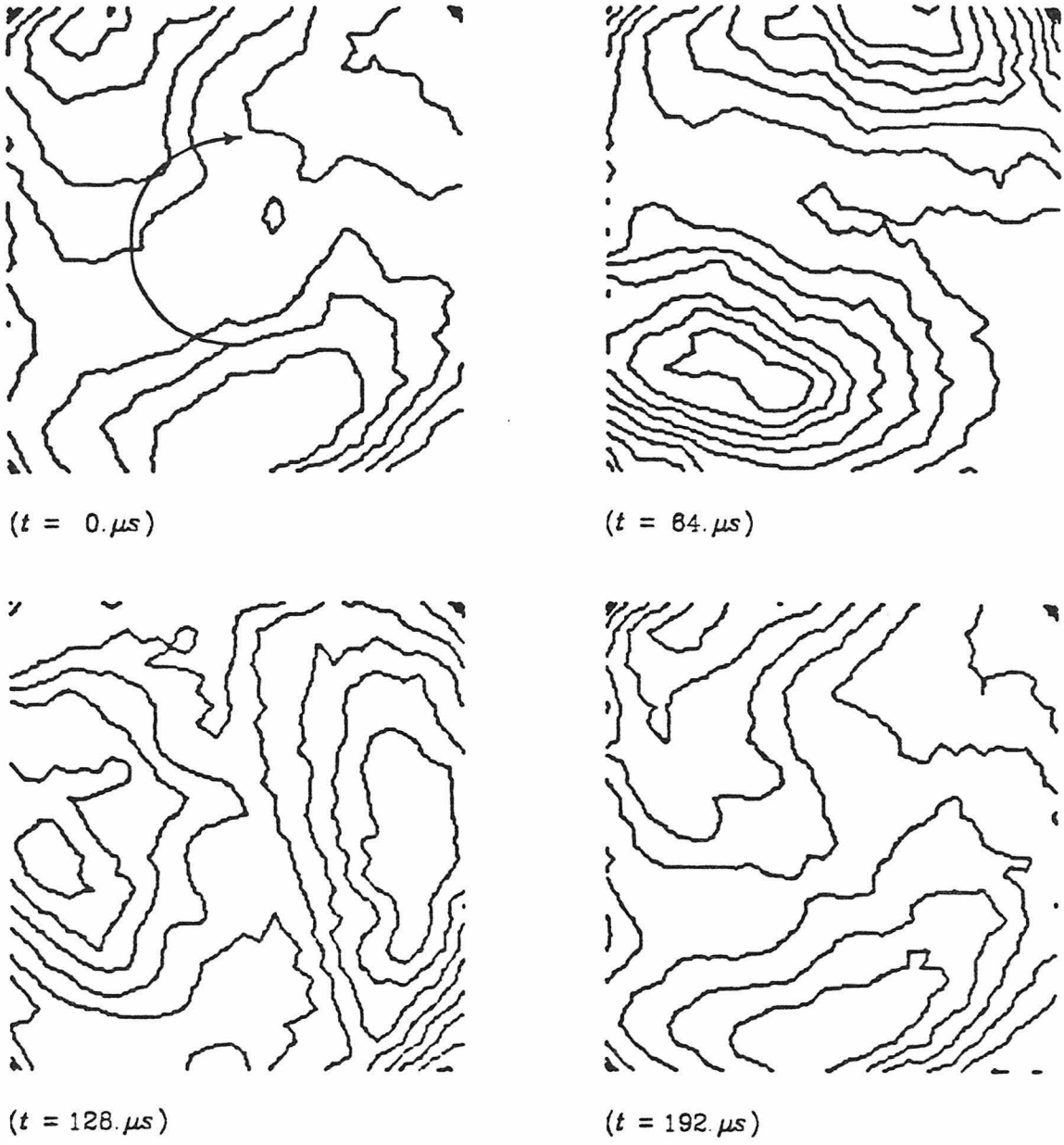

Figure 6. Contour plots of the floating potential as measured with the X-Y probe. Each plot corresponds to a different time delay with respect to a fixed reference. The electron diamagnetic drift direction is shown by the arrow, thus the mode is seen to rotate in the electron diamagnetic drift direction.

(a) density

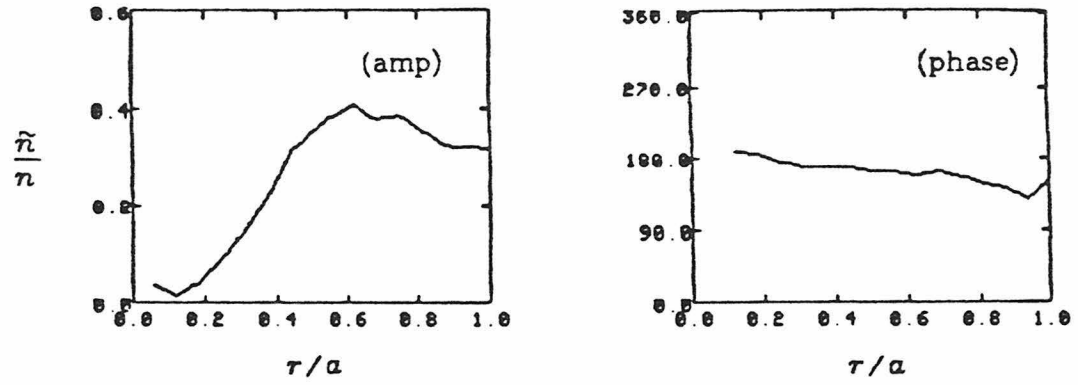

(b) temperature

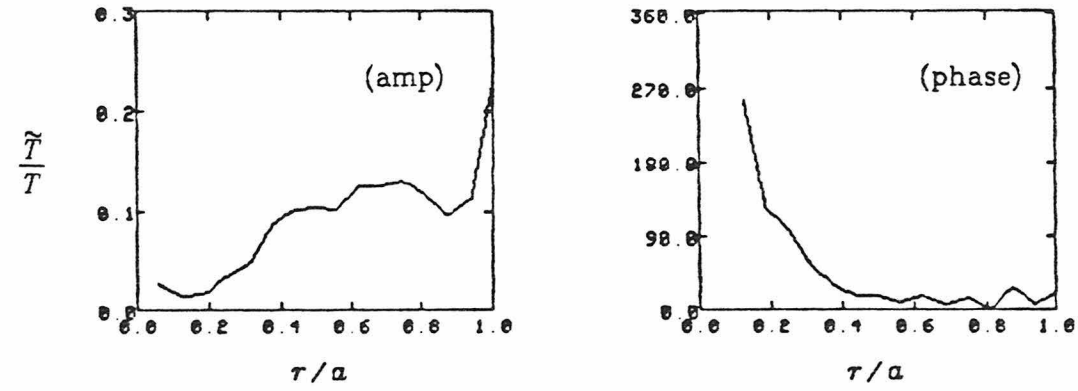

Fig. 7. Radial profiles of the amplitude and phase of the fundamental harmonic of the (a) density and (b) temperature fluctuations. The density and temperature fluctuations are normalized to the local average of the density and temperature respectively. As can be seen the temperature fluctuations are shifted $\approx 180°$ from the density fluctuations.

(a) vector potential

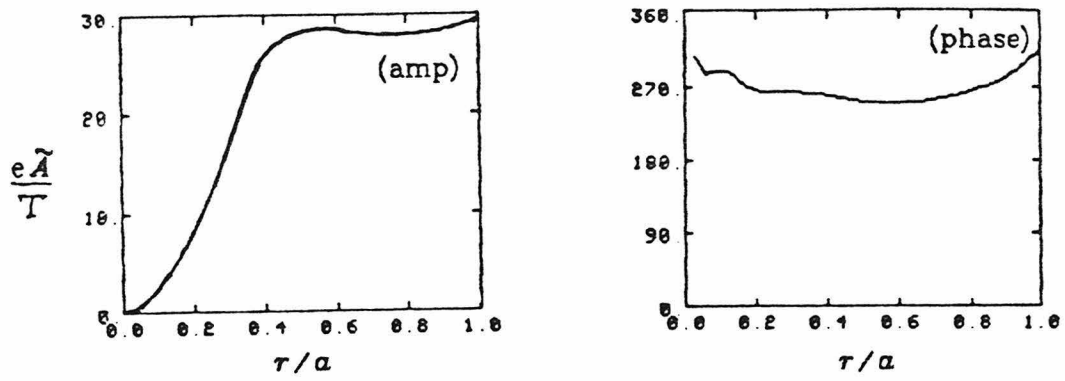

(b) space potential

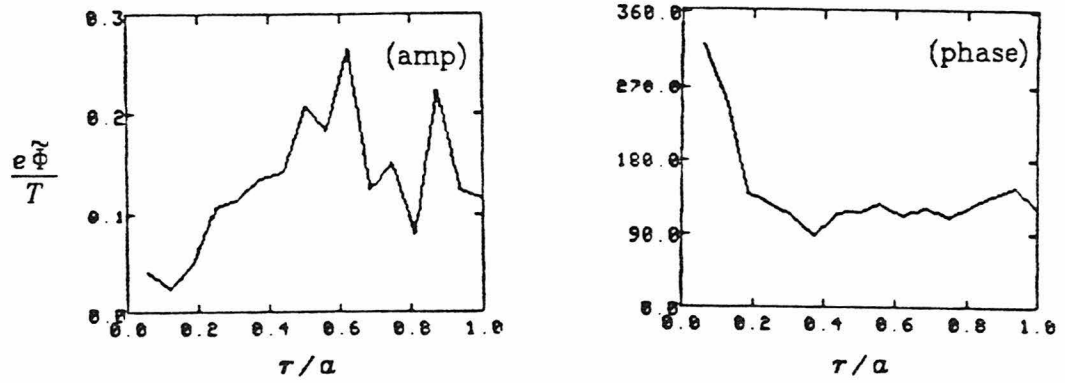

Figure 8. Radial profiles of the amplitude and phase of the fundamental harmonic of the (a) parallel vector potential and (b) space potential fluctuations. The vector potential and space potential fluctuations have been normalized to the local average electron temperature.

(a) ratio of $\frac{\omega}{c}\tilde{A}$ to $k_\parallel \tilde{\Phi}$

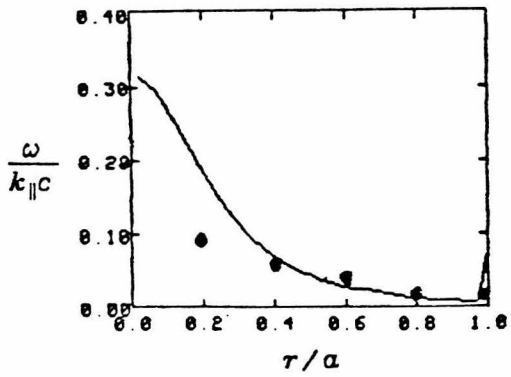

(b) variation of $k_\parallel$ with minor radius

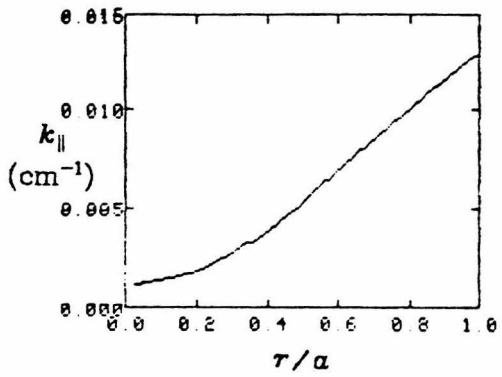

Figure 9. In figure 9(a) is the ratio of the inductive component of the parallel electric field to the electrostatic component. The ratio varies from ≈ 0.1 at the center of the plasma to ≈ 0.03 at $r/a = 0.8$. This ratio is a measure of the strength of the coupling of the drift and Alfven branches. The solid curve is the theoretical prediction and the solid circles are from experimental measurements. Figure 9(b) shows the variation of the parallel wavevector with the minor radius. The amplitude of the electric field fluctuations becomes very small near the plasma center, therefore the discrepancy between the theoretical and experimental measurements in this region is not significant.

III THEORY

A Introduction

In this chapter a theoretical model will be derived and its predictions will be compared to the experimental measurements discussed in the previous chapter. The experimental measurements showed that there were strong, coupled density and magnetic fluctuations. The fluctuations were low frequency, $\omega \ll \omega_{ci}$, coherent, with very low poloidal mode numbers (m=1,2,3). The theoretical model will deal with the coupling of the density to the magnetic fluctuations. As this is a low frequency mode, an approach using the two-fluid equations is adequate. Inclusion of kinetic effects might destabilize the mode, as for the current driven drift wave case[18].

There are two branches of the low frequency dispersion relation for warm, magnetized plasmas, the shear Alfven (or tearing) branch and the ion acoustic (or drift) branch. These branches are decoupled for low β_T, but for high β_T plasmas ($\beta_T \gg \frac{m_e}{m_i}$) or for modes with a parallel phase velocity approaching the Alfven velocity, the coupling between the branches becomes important. It is this coupling that the present work will address.

The equations used in this model are an extension of those used previously by other authors[3-6] to describe high m drift and drift-Alfven modes. These high m modes are found to be localized to regions near the rational surface; the geometry may then be simplified to that of an infinite sheared slab. In the present work it is necessary to include the full bounded sheared cylindrical geometry because the radial wavelength is of order of the machine minor radius. The equations will also include the current gradient terms, which are important for determining the stability of low m tearing modes, and will include temperature fluctuations in a manner similar to that of Ellis and Motley[19].

These equations are valid for the description of modes with frequencies much below the ion cyclotron frequency, ω_{ci}, and for plasma parameters consistent with those found in tokamak edge plasmas or in small tokamaks such as Encore. The reduced equations will be a set of three coupled equations relating the space potential, $\tilde{\Phi}$, the parallel component of the vector potential $\tilde{A}$, and the fluctuations in density $\tilde{n}$.

Moderate plasma β_T is assumed, i.e., $\frac{m_e}{m_i} \ll \beta_T \ll 1$. Thus, the coupling of the drift and Alfven branches is important, but the perpendicular components of the inductive electric field may be ignored[16], i.e., $\mathbf{E}_\parallel = -\nabla_\parallel \tilde{\Phi} - \frac{1}{c}\frac{\partial}{\partial t}\tilde{\mathbf{A}}_\parallel$, but $\mathbf{E}_\perp = -\nabla_\perp \tilde{\Phi}$. The mode frequency is assumed to lie in the range $\nu_{ie} \ll \omega \ll \omega_{ci}, \nu_{ei}$. Fluctuations in electron temperature, $\tilde{T}$, which were observed in the Encore experiments, are included in an ad hoc fashion. The ions are assumed cold and the toroidal plasma will be approximated by a straight cylinder; the toroidal direction corresponds to $\hat{z}$ and the poloidal direction to $\hat{\theta}$.

B The Two-Fluid Equations

The equations used in this derivation are the two-fluid equations. A plasma equilibrium is chosen to satisfy these equations and the linearized equations are found by perturbing about the equilibrium and keeping terms only to first order. The momentum and continuity equations (in cgs units) are:

$$0 = -e\left(\mathbf{E} + \frac{1}{c}\mathbf{v}_e \times \mathbf{B}\right) - \frac{1}{n}\nabla P - \sigma \nabla_\parallel T + \frac{m_e \nu_{ei}}{ne}\mathbf{J}_\parallel \qquad (3.1a)$$

$$m_i \frac{d\,\mathbf{v}_i}{dt} = e\left(\mathbf{E} + \frac{1}{c}\mathbf{v}_i \times \mathbf{B}\right) - \frac{m_e \nu_{ei}}{ne}\mathbf{J}_\parallel \qquad (3.1b)$$

$$\frac{\partial n_a}{\partial t} + \nabla \cdot (n_a \mathbf{v}_a) = 0 \qquad (a = e, i) \qquad (3.1c,d)$$

The term $\sigma \nabla_{\|} T$ in Eq. (3.1a) is the thermal force of Braginski[13,20]. This term arises from the temperature dependance of the collision frequency. In the presence of a gradient in the temperature, the electrons coming from the hotter region of the plasma will exert less drag on the ions than those from the cooler region. The value of σ is given by Braginski as 0.71 for $Z = 1$ and it increases slowly with Z until $\sigma = 1.5$ for $Z = \infty$. For $Z = 3-6$, $\sigma \approx 1$.

The equilibrium magnetic field is assumed to be azimuthally symmetric;

$$\mathbf{B}_0 = B_z \, \hat{\mathbf{z}} + B_\theta(r) \, \hat{\boldsymbol{\theta}} \tag{3.2a}$$

and the equilibrium plasma current density is

$$\mathbf{J}_0(r) = \mathbf{J}_D(r) + \mathbf{J}_{OH}(r) \tag{3.2b}$$

where $\mathbf{J}_D(r)$ is the diamagnetic current

$$\mathbf{J}_D(r) \approx c \, \frac{P'(r)}{B_z} \, \hat{\theta}$$

and J_{OH} is the force-free ohmic heating current

$$\mathbf{J}_{OH}(r) = J_{\|0}(r) \, \hat{b} \, . \qquad \left(\hat{b} = \frac{\mathbf{B}}{B}\right)$$

The perturbations are assumed to have the following form

$$F(r,\theta,z) = f(r) \, e^{i(m\theta - k_z z - \omega t)} \, .$$

Because of the low β_T assumption, fluctuations in the parallel magnetic field can be neglected[16], thus $\tilde{\mathbf{B}} = \tilde{\mathbf{B}}_\perp = \nabla \times \tilde{A} \hat{b}$, so that only $\tilde{\mathbf{A}}_{\|}$ is necessary. Here, parallel will be taken to mean parallel to the equilibrium magnetic field. The collision frequency is assumed to have the following dependence on density and temperature

$$\nu_{ei} \propto n \, T^{-\frac{3}{2}} \, . \tag{3.3}$$

The linearized versions of Eqs. (3.1a)-(3.1d) are:

$$0 = -ne\left(-\nabla\tilde{\Phi} + i\frac{\omega}{c}\tilde{A}\,\hat{b}\right) - \frac{e}{c}\tilde{\Gamma}_e \times \mathbf{B}_0 + \frac{1}{c}\mathbf{J}_0 \times \tilde{\mathbf{B}}$$
$$- \nabla\tilde{P} - .71\,n\nabla\tilde{T} - \frac{cm_e\nu_{ei}}{4\pi e}\nabla_\perp^2\tilde{A}\hat{b} - \frac{3m_e\nu_{ei}}{2e}J_{\|0}(r)\left(\frac{\tilde{T}}{T}\right)\hat{b} \qquad (3.4a)$$

$$-i\,\omega m_i\tilde{\Gamma}_i = ne\left(-\nabla\tilde{\Phi} + i\frac{\omega}{c}\tilde{A}\,\hat{b}\right) + \frac{e}{c}\tilde{\Gamma}_i \times \mathbf{B}_0$$
$$+ \frac{cm_e\nu_{ei}}{4\pi e}\nabla_\perp^2\tilde{A}\hat{b} + \frac{3m_e\nu_{ei}}{2e}J_{\|0}(r)\left(\frac{\tilde{T}}{T}\right)\hat{b} \qquad (3.4b)$$

$$-i\,\omega\tilde{n}_{e,i} + \nabla\cdot\tilde{\Gamma}_{e,i} = 0 \qquad (3.4c,d)$$

where $\tilde{\Gamma}_{e,i}$ are the perturbed electron and ion fluxes, and the following relationship has been used:

$$\tilde{\mathbf{J}}_\| = \frac{c}{4\pi}(\nabla\times\nabla\times\tilde{\mathbf{A}})_\| = -\frac{c}{4\pi}\nabla_\perp^2\tilde{A}\,\hat{b}\,. \qquad (3.5)$$

Based on experimental measurements, the electron temperature fluctuations can be approximated as

$$\frac{\tilde{T}}{T} \approx -(1-\gamma)\frac{\tilde{n}}{n} = -\frac{(1-\gamma)}{\gamma}\frac{\tilde{P}}{P} \qquad (3.6)$$

where $\gamma \approx \frac{1}{2}$. This is mathematically equivalent to the assumption of an adiabatic-like equation of state where

$$P \propto n^\gamma.$$

An adiabatic equation of state was used by Tang and Luhmann[10] in a study of drift and drift-Alfven waves in a linear arcjet device. They chose $\gamma = 5/3$ which results in a temperature fluctuation in phase with the density fluctuations, in contrast to what was observed for the modes in Encore. Equations (3.4a), (3.4b), (3.4c), (3.4d) and Eq. (3.6) form a closed set of equations for $\tilde{n}$, $\tilde{\Phi}$, $\tilde{A}$ and the perpendicular electron and ion fluxes. These equations will now be reduced (with suitable approximations) to (i) the linearized parallel electron momentum

equation, (ii) the ion response equation and (iii) the quasi-neutrality condition, a set of three second order differential equations in the variables $\tilde{n}$, $\tilde{\Phi}$ and $\tilde{A}$.

C The Parallel Electron Momentum Equation

The parallel component of Eq. (3.4a) is

$$0 = -(-ik_{\|}\tilde{\Phi} + i\frac{\omega}{c}\tilde{A}) + i\frac{\omega_{*p}}{c}\tilde{A} - ik_{\|}\frac{\alpha\tilde{P}}{\gamma ne} - \frac{cm_e\nu_{ei}}{4\pi ne^2}\nabla_{\perp}^2\tilde{A} + \kappa_o\frac{\alpha\tilde{P}}{\gamma ne} \quad (3.7)$$

where the following definitions have been introduced (the prime indicates a derivative with respect to r):

$$\omega_{*p} \equiv -\frac{m}{r}\frac{c(nT_e)'}{neB} \quad , \quad (3.8a)$$

$$\kappa_o \equiv \frac{3(1-\gamma)}{2\alpha}\frac{m_e\nu_{ei}}{ne}\frac{J_{\|o}(r)}{T} = \frac{3(1-\gamma)}{2\alpha}\left[\frac{eE_{\|o}}{T_e}\right] \quad , \quad (3.8b)$$

$$\alpha \equiv \gamma - \sigma(1-\gamma) \quad ,$$

and

$$k_{\|} = \mathbf{k}\cdot\hat{b} \quad . \quad (3.8c)$$

Here ω_{*p} is the electron diamagnetic drift frequency, κ_o^{-1} is the distance over which an electron picks up T_e of energy from the loop voltage, and $k_{\|}$ is the parallel component of the wave number. At a mode rational surface $k_{\|}$ will go through zero. If $\kappa_o \approx k_{\|}$, then temperature fluctuations must be retained when calculating fluctuations in plasma current.

After rearranging, Eq. (3.7) becomes

$$-ik_{\|}\tilde{\Phi} + ik_{\|}\frac{\alpha\tilde{P}}{\gamma ne} - \kappa_o\frac{\alpha\tilde{P}}{\gamma ne} = \frac{i}{c}(\omega_{*p} - \omega + i\frac{m_e\nu_{ei}c^2}{4\pi ne^2}\nabla_{\perp}^2)\tilde{A} \quad . \quad (3.9)$$

Defining a new variable,

$$\tilde{\Psi} \equiv \tilde{\Phi} - \frac{\alpha\tilde{P}}{\gamma ne} \quad , \quad (3.10)$$

so Eq. (3.9) becomes

$$-\bar{k}_{\parallel} c \tilde{\Psi} = (\omega_{*p} - \omega + i \frac{\nu_{ei} c^2}{\omega_{pe}^2} \nabla_{\perp}^2) \tilde{A} - i\kappa_0 c \tilde{\Phi} \tag{3.11}$$

where

$$\bar{k}_{\parallel} \equiv (k_{\parallel} + i\kappa_0).$$

Equation (3.11) describes how the induced electric field, the collisional drag and the interaction of the equilibrium perpendicular current with fluctuating magnetic fields all act to modifiy the free movement of electrons along the magnetic field. If the r.h.s of Eq. (3.11) were zero, $\tilde{\Psi}$ would vanish, i.e., the electrons would free-stream along the magnetic field, and would have a Boltzmann distribution, $\frac{\alpha \tilde{P}}{\gamma P} = \frac{e\tilde{\Phi}}{T}$. Thus Eq. (3.11) describes the extent to which the electrons do not have a Boltzmann distribution.

D The Ion Response Equation

The ion response is found by solving Eq. (3.4b) for the divergence of the ion flux and then substituting this into the ion continuity equation, Eq. (3.4d). For argon plasmas the parallel ion flux terms, which give the ion sound speed corrections, are negligible and will not be included in this derivation.

Since $\omega \ll \omega_{ci}$, the ion perpendicular flux from Eq. (3.4b) is the sum of the ion $\mathbf{E}\times\mathbf{B}$ and polarization drifts;

$$\tilde{\Gamma}_{\perp i} = -\frac{nc}{B^2} \nabla_{\perp} \tilde{\Phi} \times \mathbf{B}_0 + i \frac{\omega}{\omega_{ci}} \frac{nc}{B} \nabla_{\perp} \tilde{\Phi} \tag{3.12}$$

The divergence of the perpendicular ion flux is

$$\nabla \cdot \tilde{\Gamma}_{\perp i} = -\nabla n_0 \cdot \frac{c}{B^2} \nabla \tilde{\Phi} \times \mathbf{B}_0 - \frac{nc}{B^2} \nabla \cdot \nabla \tilde{\Phi} \times \mathbf{B}$$
$$+ i \frac{\omega}{\omega_{ci}} \frac{c}{B} \nabla n \cdot \nabla_{\perp} \tilde{\Phi} + in \frac{\omega}{\omega_{ci}} \frac{c}{B} \nabla \cdot \nabla_{\perp} \tilde{\Phi} \tag{3.13}$$

The first term introduces a frequency similar to the diamagnetic drift frequency, but dependent on the gradient in density (rather than pressure);

$$-\nabla n_0 \cdot \frac{c}{B^2}\nabla\tilde{\Phi}\times\mathbf{B} = \frac{ine}{T}\omega_{*n}\tilde{\Phi}, \tag{3.14}$$

where $\omega_{*n} \equiv -\frac{m}{r}\frac{cT}{eB}\frac{n'}{n}$.

The second term comes from the **E**×**B** and pressure gradient drifts associated with the poloidal field and can be expressed as

$$-\frac{nc}{B^2}\nabla\cdot\nabla\tilde{\Phi}\times\mathbf{B} = \frac{ine}{T}\frac{1}{2}\beta_T k_\parallel v_{\parallel 0}\tilde{\Phi} \tag{3.15}$$

This term is smaller than the first by a factor of $\beta_T \frac{k_\parallel v_{\parallel 0}}{\omega_{*n}}$, and can be neglected as $\beta_T \ll 1$ and $k_\parallel v_{\parallel 0} \approx \omega_{*p}$. The third term is smaller than the first by $\frac{\omega}{\omega_{ci}}$ and thus is also neglected. The divergence of the ion flux is then

$$\frac{i}{n}\nabla\cdot\tilde{\Gamma}_{\perp i} = -\frac{e}{T}(\omega_{*n} + \omega\rho^2{}_s\nabla_\perp^2)\tilde{\Phi} \tag{3.16}$$

where $\rho_s^2 = \frac{T}{m_i\omega_{ci}{}^2}$. With the above result and Eq. (3.6), the linearized ion continuity equation becomes

$$-\omega\frac{\tilde{n}}{n} = -\frac{e}{T}(\omega_{*n} + \omega\rho^2{}_s\nabla_\perp^2)\tilde{\Phi}$$

or, using Eqs. (3.6) and (3.10),

$$-\frac{\omega}{\alpha}\tilde{\Psi} = (\omega_{*n} - \frac{\omega}{\alpha} + \omega\rho^2{}_s\nabla_\perp^2)\tilde{\Phi} \tag{3.17}$$

E The Quasi-Neutrality Condition

Quasi-neutrality implies that

$$\nabla\cdot\tilde{\mathbf{J}} = 0. \tag{3.18}$$

In terms of the perpendicular ion and electron fluxes and the parallel current, this becomes

$$\nabla\cdot(\tilde{\Gamma}_{\perp i}-\tilde{\Gamma}_{\perp e})=-\frac{1}{e}\nabla\cdot\tilde{\mathbf{J}}_{\parallel}. \tag{3.19}$$

The divergence of the ion flux is already known [Eq. (3.16)]. The perpendicular electron flux is found by solving Eq. (3.4a) for $\tilde{\Gamma}_{\perp e}$;

$$\begin{aligned}\tilde{\Gamma}_{\perp e} &= -\frac{nc}{B^2}\nabla_\perp\tilde{\Phi}\times\mathbf{B}_0+\frac{c}{eB^2}\nabla_\perp\tilde{P}\times\mathbf{B}_0-\frac{J_{\parallel 0}(r)}{eB}\tilde{\mathbf{B}}_\perp\\ &=\tilde{\Gamma}_e^{(E\times B)}+\tilde{\Gamma}_e^{(\nabla P\times B)}+\tilde{\Gamma}_e^{J_0}\end{aligned} \tag{3.20}$$

The terms in Eq. (3.20) are, respectively, the **E×B** drift, the pressure gradient drift and a term resulting from the interaction of the equilibrium electron flow with the perturbed magnetic fields. (This last term drives the classical tearing instability[21].) The divergence of the **E×B** drift has previously been calculated for the ions and is

$$\frac{i}{n}\nabla\cdot\tilde{\Gamma}_{\perp e}^{(E\times B)}=-\frac{e}{T}\omega_{*n}\tilde{\Phi} \tag{3.21}$$

The second term is smaller by β_T than the first term and is dropped [cf. discussion of Eq. (3.15)]. The last term is

$$\frac{i}{n}\nabla\cdot\tilde{\Gamma}_e^{J_0}=\frac{-i}{n}\nabla\left(\frac{J_{\parallel 0}(r)}{eB}\right)\cdot\tilde{\mathbf{B}}_\perp=\frac{e}{T}\frac{m}{\tau}\frac{T}{ne^2}\frac{J_{\parallel 0}'(r)}{B}\tilde{A}_\parallel \tag{3.22}$$

The total divergence of the perpendicular electron flux is then

$$\frac{i}{n}\nabla\cdot\tilde{\Gamma}_{\perp e}=-\frac{e}{T}\left(\omega_{*n}\tilde{\Phi}+\omega_J\tilde{A}\right). \tag{3.23}$$

where ω_J has been defined as

$$\omega_J\equiv-4\pi k_\perp\lambda_{de}^2\frac{J_{\parallel 0}'(r)}{B}. \tag{3.24}$$

Combining this result with the divergence of the perpendicular ion flux, Eq. (3.16) and Ampere's law, Eq. (3.5) gives

$$\frac{i}{n}\nabla\cdot(\tilde{\Gamma}_{\perp i}-\tilde{\Gamma}_{\perp e}) = \frac{e}{T}(\omega_J\tilde{A}-\omega\rho_s^2\nabla_\perp^2\tilde{\Phi})$$
$$= -\frac{i}{ne}\nabla\cdot\tilde{\mathbf{J}}_\parallel$$
$$= -(\frac{e}{T})k_\parallel c\lambda_d^2\nabla_\perp^2\tilde{A}.$$

Thus, the quasi-neutrality condition can be written as

$$\omega\rho_s^2\nabla_\perp^2\tilde{\Phi} = k_\parallel c\lambda_d^2\nabla_\perp^2\tilde{A} + \omega_J\tilde{A}. \tag{3.25}$$

F Simplification of the Reduced Equations

Equations (3.11), (3.17) and (3.25) are a complete set of equations. They will now be rewritten in a form more convenient for the numerical and analytical work which follows. Using Eq. (3.11) to eliminate $\tilde{\Psi}$ from Eq. (3.17) yields

$$-\frac{\omega}{\alpha\bar{k}_\parallel c}\left[(\omega_{*p}-\omega+i\frac{\nu_{ei}c^2}{\omega_{pe}^2}\nabla_\perp^2)\tilde{A}-i\kappa_o c\tilde{\Phi}\right]$$
$$= (\frac{\omega}{\alpha}-\omega_{*n}-\omega\rho_s^2\nabla_\perp^2)\tilde{\Phi}. \tag{3.26}$$

Equations (3.25) and (3.26) may be written in a more symmetric form. Using Eq. (3.25) to substitute for $\omega\rho_s^2\nabla_\perp^2\tilde{\Phi}$ in Eq. (3.26) gives

$$-\frac{\omega}{\alpha\bar{k}_\parallel c}\left[(\omega_{*p}-\omega+i\frac{\nu_{ei}c^2}{\omega_{pe}^2}\nabla_\perp^2)\tilde{A}-i\kappa_o c\tilde{\Phi}\right]$$
$$= (\frac{\omega}{\alpha}-\omega_{*n})\tilde{\Phi}-(\omega_J+k_\parallel c\lambda_{de}^2\nabla_\perp^2)\tilde{A} \tag{3.27}$$

This equation may now be solved for $\nabla_\perp^2\tilde{A}$ to get

$$(\alpha k_\parallel\bar{k}_\parallel - i\frac{\omega\nu_{ei}}{V_{Te}^2})\lambda_{de}^2\nabla_\perp^2\tilde{A} = \frac{\alpha\bar{k}_\parallel}{c}(\frac{\omega}{\alpha}-\omega_{*n})\tilde{\Phi}$$
$$+\left[\frac{\omega}{c^2}(\omega_{*p}-\omega)-\frac{\alpha\bar{k}_\parallel}{c}\omega_J\right]\tilde{A}-i\frac{\kappa_o c}{\omega}(\frac{\omega}{c})^2\tilde{\Phi} \tag{3.28}$$

or, in a form similar to that of Ref. 4,

$$\nabla_\perp^2\tilde{A} = \sigma(r)\frac{\omega}{c}\left[(\frac{\omega}{c}\Omega_2-\alpha\frac{\omega_J}{\omega}\bar{k}_\parallel)\tilde{A}-(\alpha\Omega_1\bar{k}_\parallel+i\kappa_o)\tilde{\Phi}\right] \tag{3.29}$$

where the following definitions have been used:

$$\Omega_1 = \frac{\omega_{*n}}{\omega} - \frac{1}{\alpha} \qquad \Omega_2 = \frac{\omega_{*p}}{\omega} - 1$$

$$\sigma(r) = \frac{1}{\alpha k_\parallel \bar{k}_\parallel D_\parallel - i\,\omega}\left(\frac{4\pi}{\eta_s}\right) \qquad D_\parallel = \frac{v_T^2}{\nu_{ei}}$$

Here $D_\parallel$ is the parallel electron diffusion coefficient, $\eta_s \equiv \frac{m_e \nu_{ei}}{ne^2}$ is the Spitzer resistivity, and the function $\sigma(r)$ is the generalized dimensionless conductivity in the semi-collisional ordering of Drake and Lee[22], sometimes referred to as the semi-hydrodynamic approximation[6].

A similar equation can be written for $\nabla_\perp^2 \tilde{\Phi}$. Equation (3.29) is used to substitute for $\nabla_\perp^2 \tilde{A}$ in Eq. (3.25), resulting in

$$\lambda_{de}{}^2 \sigma(r)\,\frac{\omega}{c}\left[\left(\frac{\omega}{c}\Omega_2 - \frac{\alpha\omega_J}{\omega}\bar{k}_\parallel\right)\tilde{A} - \left(\alpha\Omega_1\bar{k}_\parallel + i\kappa_o\right)\tilde{\Phi}\right]$$
$$= \frac{1}{k_\parallel c}\left(\omega\rho_s{}^2\nabla_\perp^2\tilde{\Phi} - \omega_J\tilde{A}\right) \qquad (3.30)$$

which, with the previous definitions, may be written as

$$\nabla_\perp^2\tilde{\Phi} = -\sigma(r)\left(\frac{V_A}{c}\right)^2\left[\left(\alpha\Omega_1 k_\parallel\bar{k}_\parallel + i\kappa_o k_\parallel\right)\tilde{\Phi} - \left(\frac{\omega}{c}\Omega_2 k_\parallel - i\frac{\omega_J}{D_\parallel}\right)\tilde{A}\right]. \qquad (3.31)$$

The final step is to use Eqs. (3.11) and (3.29) to find a simple equation for the density fluctuations in terms of $\tilde{\Phi}$ and $\tilde{A}$. Substituting for $\nabla_\perp^2\tilde{A}$ in Eq. (3.11)

$$-\frac{\bar{k}_\parallel c}{\omega}\tilde{\Psi} = \Omega_2\tilde{A} - \frac{i\kappa_o c}{\omega}\tilde{\Phi}$$

$$+ i\left(\frac{\eta_s c^2}{4\pi\omega}\right)\sigma(r)\,\frac{\omega}{c}\left[\left(\frac{\omega}{c}\Omega_2 - \alpha\frac{\omega_J}{\omega}\bar{k}_\parallel\right)\tilde{A} - \left(\alpha\Omega_1\bar{k}_\parallel + i\kappa_o\right)\tilde{\Phi}\right] \qquad (3.32)$$

which may then be simplified further

$$-\tilde{\Psi} = \alpha\lambda_{de}{}^2\sigma(r)\left[\left(\frac{\omega}{c}\Omega_2 k_\parallel - i\frac{\omega_J}{D_\parallel}\right)\tilde{A} - \left(i\kappa_o k_\parallel + i\frac{\omega}{D_\parallel}\Omega_1\right)\tilde{\Phi}\right]. \qquad (3.33)$$

Equations (3.29), (3.31) and (3.33) make up the final set of equations which will be used in the numerical code as discussed in the following sections.

G Approximate Analytical Solution

Before proceeding with the discussion of the numerical results, an approximate analytical solution to Eqs. (3.29), (3.31) and (3.33) will be found. This will clarify the situation regarding the numbers of solutions and the branch to which they belong. An analytic dispersion relation may be found under the following assumptions: (i) the density profile is Gaussian, (ii) the electron temperature is constant, (iii) the plasma current profile is flat, i.e., $k_\parallel$ = const. and (iv) the dependence of the Alfven velocity on minor radius can be neglected. With these approximations, $\omega_{*n} = \omega_{*p}$ = const., $\alpha = 1$, $\Omega_1 = \Omega_2 = \Omega$, $\omega_J = 0$ and $\bar{k}_\parallel = k_\parallel$ and so Eqs. (3.29) and (3.31) become:

$$\rho_s^2 \nabla_\perp^2 \tilde{\Phi} = -k_\parallel^2 \lambda_{de}^2 \sigma(r) \Omega \left[\tilde{\Phi} - \frac{\omega}{k_\parallel c} \tilde{A} \right] \tag{3.34}$$

$$\rho_s^2 \nabla_\perp^2 \tilde{A} = -\frac{c^2}{V_A^2} k_\parallel \lambda_{de}^2 \sigma(r) \Omega \left(\frac{\omega}{c}\right) \left[\tilde{\Phi} - \left(\frac{\omega}{k_\parallel c}\right) \tilde{A} \right] \tag{3.35}$$

where all coefficients are now constant. These equations may also, for simplicity, be written in a matrix form as

$$\rho_s^2 \nabla_\perp^2 \begin{bmatrix} \tilde{\Phi} \\ \tilde{A} \end{bmatrix} + \Omega f \begin{bmatrix} 1 & -\frac{\omega}{k_\parallel c} \\ \frac{\omega c}{k_\parallel V_A^2} & -\left(\frac{\omega}{k_\parallel V_A}\right)^2 \end{bmatrix} \begin{bmatrix} \tilde{\Phi} \\ \tilde{A} \end{bmatrix} = 0 \tag{3.36}$$

where

$$f \equiv k_\parallel^2 \lambda_{de}^2 \sigma(r) = \frac{1}{1 - i\,\omega \tau_\parallel}, \tau_\parallel \equiv \frac{1}{k_\parallel^2 D_\parallel}. \tag{3.37}$$

The eigenvalues for the matrix are,

$$\lambda_{1,2} = \begin{cases} \left(1 - \left(\frac{\omega}{k_\parallel V_A}\right)^2\right) \\ 0 \end{cases} \tag{3.38}$$

so if the appropriate transformations to diagonalize the matrix are carried out, the result is two decoupled equations of the form

$$\rho_s^2 \nabla_\perp^2 \left[\tilde{\Phi} - \frac{\omega}{k_\parallel c}\tilde{A}\right] + \Omega f \left[1 - (\frac{\omega}{k_\parallel V_A})^2\right]\left[\tilde{\Phi} - \frac{\omega}{k_\parallel c}\tilde{A}\right] = 0 \qquad (3.39)$$

$$(\Omega f)^{-1} \rho_s^2 \nabla_\perp^2 \left(-\frac{\omega c}{k_\parallel V_A^2}\tilde{\Phi} + \tilde{A}\right) = 0 \qquad (3.40)$$

Equation (3.39) has solutions of the form $e^{im\theta}J_m(k_r r)$, and the standard[23] drift-Alfven dispersion relation is then recovered:

$$(1 - i\omega\tau_\parallel)\,\omega k_r^2 \rho_s^2 = (\omega_* - \omega)\left(1 - (\frac{\omega}{k_\parallel V_A})^2\right) \qquad (3.41)$$

where k_r is defined as x_j^m / a and x_j^m is the j'th zero of the m'th Bessel function. Solutions to Eq. (3.41) are graphed in Fig. 10, with the assumption that $\omega\tau_\parallel \ll 1$ and that $b = 1.5$. Equation (3.41) is cubic in ω; the three roots are, with the assumptions that $\omega\tau_\parallel \ll 1$ and $k_\parallel V_A \gg \omega_*$, given as

$$\omega_1 \approx \frac{\omega_*}{1+b}\left[1 - \frac{\omega_*^2}{\omega_A^2}\frac{b}{(1+b)^3}\right] + i\,\frac{\omega_*^2 \tau_\parallel b}{(1+b)^3} \qquad (3.42)$$

$$\omega_{2,3} \approx \pm (1+b)^{\frac{1}{2}}\omega_A + \frac{b}{2(1+b)}\omega_* - \frac{1}{2} i\, b\, \omega_A^2 \tau_\parallel \qquad (3.43)$$

where $\omega_A \equiv k_\parallel V_A$ and $b \equiv k_r^2 \rho_s^2$. These solutions correspond to the two shear-Alfven solutions and the electrostatic drift wave solution. Equation (3.40) has just one root, namely $\omega = 0$ (i.e., $\Omega \to \infty$). [If the current gradient terms are kept, this solution has a non-zero frequency, ($\omega \approx 10^2$ Hz), but still too slow to be seen on the time scale of the plasma existence].

If the modes described by Eq. (3.41) exist (i.e., ω is given by Eqs. (3.42) or (3.43)), then the only way to satisfy Eq. (3.40) is to set

$$\tilde{A} = \frac{\omega c}{k_\parallel V_A^2}\tilde{\Phi}. \qquad (3.44)$$

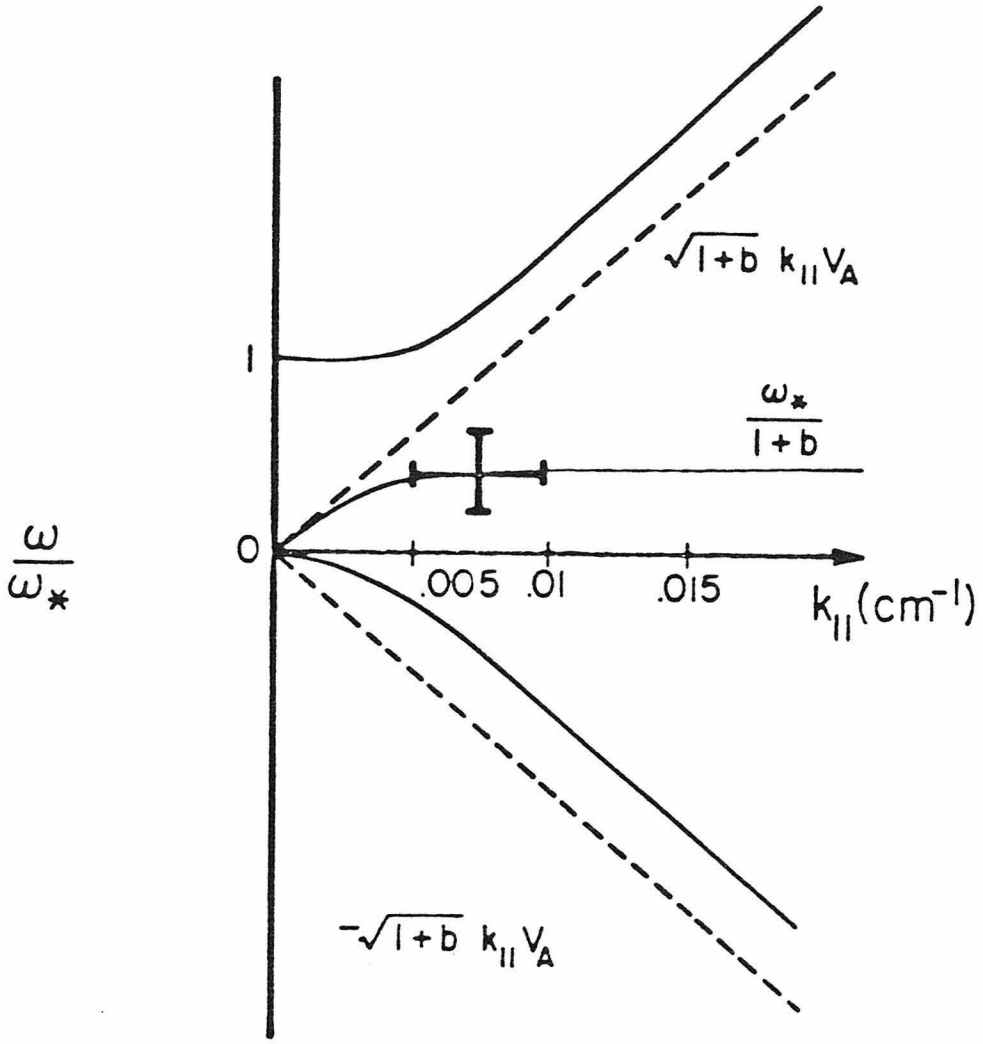

Figure 10. The analytic dispersion relation showing the coupling of the drift and Alfven branches at small $k_{||}$. The error bars show the location of the observed frequency and $k_{||}$. The width of the error bars reflects the variation of $k_{||}$ and ω_* over the range of minor radius where the mode has an appreciable amplitude (cf. Figs. 7 and 11). This figure is plotted from Eq. (3.41) assuming $b = 1.5$. The observed frequency of the mode is 5 kHz and the electron diamagnetic drift frequency is between 10 and 20 kHz.

Another relation between $\tilde{A}$ and $\tilde{\Phi}$ can be deduced as follows: Equation (3.34) reduces to the electrostatic drift wave dispersion relation when $\tilde{A} = 0$, thus the coupling of the drift to the Alfven branch is seen to be important when the inductive component of the parallel electric field becomes comparable to the electrostatic component, i.e.,

$$\frac{\omega}{c}\tilde{A} \approx k_{\parallel}\tilde{\Phi}. \tag{3.45}$$

From Eqs. (3.44) and (3.45), the condition for significant drift-Alfven coupling becomes

$$(\frac{\omega}{k_{\parallel}V_A})^2 \approx 1 \tag{3.46}$$

or

$$\beta_T \approx \left(\frac{k_{\parallel}V_{T_e}}{\omega}\right)^2 \frac{m_e}{m_i}. \tag{3.47}$$

It is the normalized magnetic fluctuation level, $\tilde{B}/B$, that is generally of interest, so using $\tilde{B}_r \approx ik_{\perp}\tilde{A}$ and $\beta_T = 8\pi n T_e / B^2$, Eq. (3.44) becomes

$$\frac{\tilde{B}}{B} \approx \frac{i}{2}\frac{k_{\perp}}{k_{\parallel}}\frac{\omega}{\omega_{ci}}\beta_T(\frac{e\tilde{\Phi}}{T}) \tag{3.48}$$

thus regaining the result derived by Kadomtsev[23]. The parameters determining the coupling of the magnetic to the electrostatic fluctuations can be, to some extent, understood through simple physical arguments. The electrostatic drift wave couples to the shear Alfven branch through the parallel motion of the electrons, which causes current, and hence, magnetic fields. In a drift wave, the electrons move parallel to the field to neutralize the local charge imbalance resulting from the differences in the perpendicular motions of the electrons and the ions. This difference in the perpendicular motions of the ions and electrons is caused by the difference in masses of these particles. For frequencies much below the cyclotron frequency, the mass of the particle can be ignored in

calculating the perpendicular response to the wave. The corrections to this response (the polarization drift) are of order ω/ω_c, so the difference between the ion and electron perpendicular motions will scale as ω/ω_{ci}, meaning that the amplitude of the parallel electron current necessary to make up for this must also scale in the same way. Likewise, the smaller $k_\parallel$ the further the electrons have to move in one wave period, and the larger the currents become. The factor of $\beta_T = 8\pi nT/B^2$ reflects the scaling of the potential fluctuations to T, the magnetic fluctuations to B and that the plasma current density scales as n and the polarization drift scales as B^{-1}.

Fluctuations in the electron temperature, not included in the above equations, can also be important in the coupling of the drift to the Alfven branch. The electron temperature fluctuations affect the local plasma conductivity, and can thus induce fluctuations in the local current density. The condition that this effect be important is that the effective force on the electrons from the change in conductivity be comparable to the force from the electric field of the drift wave. The exact condition that temperature fluctuations be important is

$$\kappa_o \equiv \frac{3(1-\gamma)}{2\alpha}\frac{eE_{\parallel o}}{T} \geq k_\parallel \qquad (3.49)$$

which means that the loop voltage, V_l, must be of the order of the electron temperature. As $V_l \approx T$ in Encore, temperature fluctuations have been included in the model, as discussed earlier. This effect will not be important in hotter tokamaks where $V_l \ll T$.

H Numerical Solution of the Equations

The full set of equations is solved for various plasma parameters using a numerical code described in Appendix A. The code uses as input the standard plasma parameters such as toroidal field, Z_{eff}, ion mass etc. It also uses multi-

parameter analytic functions to approximate the experimentally determined density and current profiles. The code uses the conductivity temperature profile, rather than the somewhat different profile obtained from the Langmuir probe measurements. The equations are not strongly sensitive to the temperature profiles and the conductivity profile is more convenient to use.

The problem is a boundary value problem, and the eigenvalues and functions are affected, to some extent, by the boundary conditions used. As the vacuum chamber wall is a very good conductor, conducting wall boundary conditions are used, i.e., (without temperature fluctuations) $\tilde{\Phi}(a) = \tilde{A}(a) = 0$. Experimentally it is observed that $\tilde{B}_r$ and hence, $\tilde{A}$, do go to zero at the wall, but that $\tilde{n}/n$ does not. The sensitivity of the solutions to the boundary conditions was checked by using several boundary conditions at the wall on $\tilde{\Phi}$, but requiring always that $\tilde{A}$ go to zero. It was found that the effects on the frequency and mode amplitudes were small, typically less than a few percent.

I Results

Numerical solutions have been found corresponding to the drift wave and the two shear-Alfven solutions of the analytic dispersion relation, Eq. (3.41) for m=2. The results of these numerical calculations for parameters consistent with the data presented in Figs. 4-9 are presented in Table I and Fig. 11. As the code is based on a linear theory and does not predict a saturation level, the numerical results must be scaled to one of the experimentally measured quantities; in this case, as $\tilde{n}/n$ is the best known of the experimental measurements, it was chosen as the point of comparison. From the data in Table 1, it is obvious that the experimental measurements are best fit by the drift-wave solution. The two shear-Alfven solutions have much larger ratios of vector potential to density fluctuations and the frequencies for the shear-Alfven solutions do not agree with

TABLE I

(comparison of theoretical predictions to experiment)

	$\frac{\tilde{n}}{n}$ (amp,phase)	$\frac{e\tilde{\Phi}}{T}$ (amp,phase)	$\frac{e\tilde{A}}{T}$ (amp,phase)	ω_r (10^4rad/s)
experiment	(.40, 0°)	(.20, 45°)	(30,−100°)	3.0
Drift wave	(.40, 0°)	(.16, 10°)	(28, 20°)	2.4
Alfven	(.40,---)	(.40,---)	(800,---)	30.0
	(.40,---)	(.04,---)	(70,---)	−15.0

Table 1. This table compares the experimental peak amplitudes, phases and frequencies of the radial eigenfunctions for $e\tilde{\Phi}/T$ and $e\tilde{A}/T$ to those predicted theoretically for for the drift wave and two shear-Alfven waves. The numerical code is based on a linear theory, so the peak amplitude of $\tilde{n}/n$ is used to scale the theoretical results. Likewise, the relative phases are measured with respect to $\tilde{n}/n$. The phases of the eigenfunctions for the two Alfven solutions vary considerably over the minor radius, thus the relative phases of $\tilde{n}/n$, $e\tilde{\Phi}/T$ and $e\tilde{A}/T$ are not well defined. The space and vector potentials have been normalized to the electron temperature.

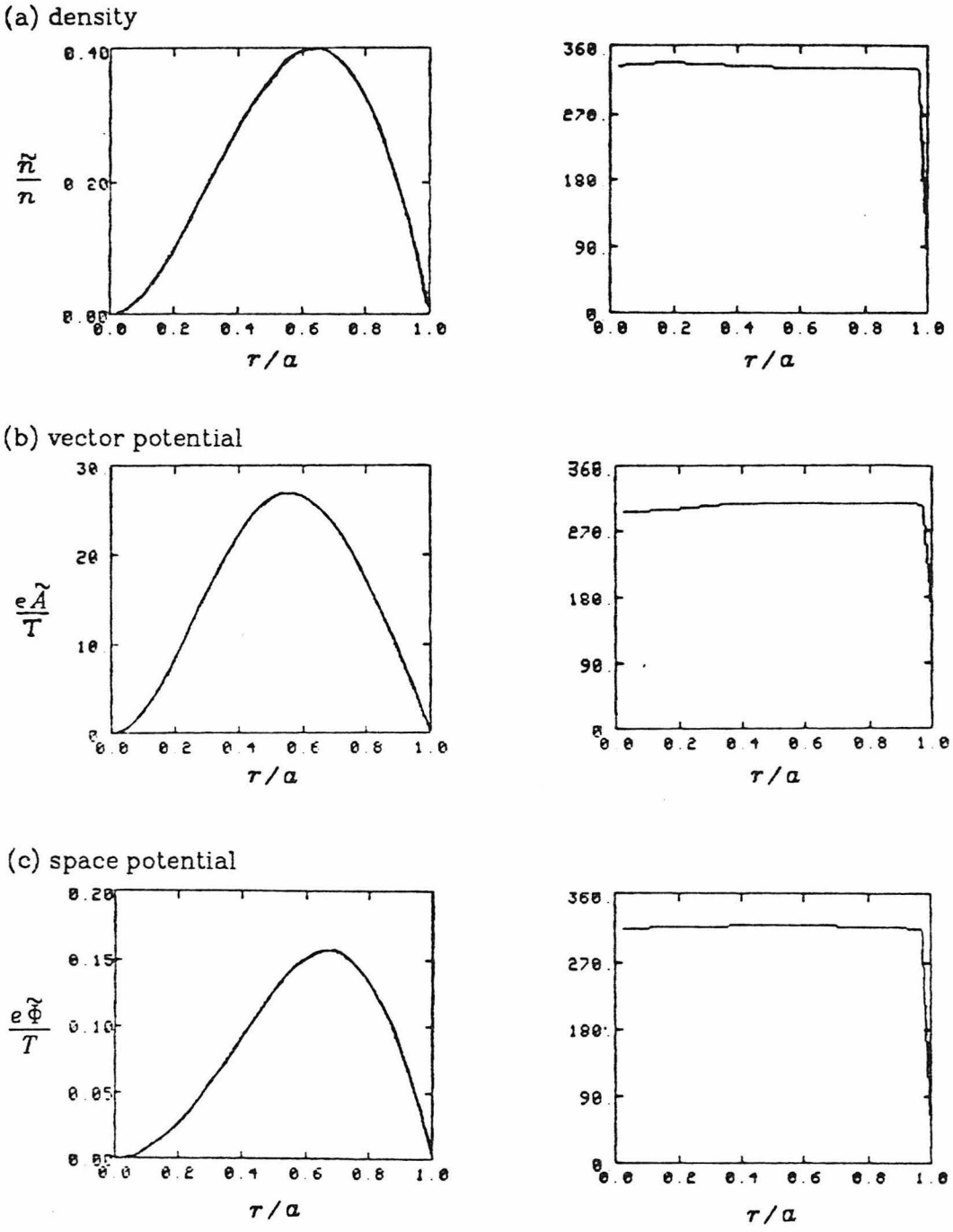

Figure 11. Radial profiles of the theoretically computed amplitude and phase of the (a) density, (b) vector potential and (c) space potential fluctuations for the m=2 drift wave solution. The amplitudes have been set by normalizing the density fluctuations to $\frac{\tilde{n}}{n} = 0.4$. The space and vector potential fluctuations are normalized to the local average electron temperature.

the observed frequency of the mode.

The profiles of the safety factor, density and electron temperature used for this solution are presented in Fig. 4. The predicted frequency of the mode was found to depend strongly (nearly linearly) on the choice of Z_{eff}. The Z_{eff} was chosen based on a comparison of the conductivity temperature [see Eq. (2.2)] and the temperature determined from the Langmuir probe I-V. The data indicate, as mentioned earlier, that Z_{eff} is a function of minor radius, and thus there is some uncertainty introduced in the choice of a constant Z_{eff} in the code. For these data, the choice of $Z_{eff} = 4.5$ was made to give a reasonable 'average' fit of the conductivity and Langmuir probe temperatures.

The other parameter which was determined from the experimental data was the ratio of $\tilde{T}/T$ to $\tilde{n}/n$. The measurements of the saturated mode gave this ratio as $\tilde{T}/T = -0.3\tilde{n}/n$. The temperature fluctuations were found to have a stabilizing effect on the mode. If the temperature fluctuations were set equal to zero, the mode was unstable with a growth rate of $\gamma = 1.3 \times 10^3$/sec. Inclusion of the temperature fluctuations resulted in a negative growth rate. If the temperature fluctuations were due to local radiative cooling, they would scale non-linearly with $\tilde{n}/n$ and would be a possible saturation mechanism for the mode.

With the above choices of parameters, the numerical results agree quite well with the experimental measurements as can be seen in Table I. The predicted frequency agrees quite well with the measured value, experimentally $f = 5.0$ kHz and theoretically $f = 4.0$ kHz. As discussed above, the uncertainties in the value of Z_{eff} mean that the predicted frequency is only good to ≈ 1 kHz. The predictions of the relative amplitudes of $\tilde{n}/n$, $e\tilde{\Phi}/T$ and $\tilde{A}$, which were not sensitive to the choice of Z_{eff}, were quite good also.

The predictions of the relative phases between the fluctuating quantities

was not quite as good. The theoretical phase shifts between $\tilde{n}/n$, $e\tilde{\Phi}/T$ and $\tilde{A}$ were all quite small. Experimentally, it was found that the space potential fluctuations led the density fluctuations by $\approx 45°$ and that the vector potential fluctuations lagged the density fluctuations by $\approx 100°$. The phase shifts (at least between $\tilde{n}/n$ and $e\tilde{\Phi}/T$) are related to the stability of the mode and the theory has neglected at least one important destabilizing effect, the resonant interaction of the waves with the current carrying electrons[18]. The growth rate due to these effects in the absence of collisions and in a local theory is given by

$$\frac{\omega_i}{\omega_r} \approx \left(\frac{\pi}{2}\right)^{\frac{1}{2}} \left[\frac{v_d}{(1+b)v_T} + \frac{\omega_* b}{(1+b)^2} \right] \approx .1 \qquad (3.50)$$

It seems unlikely, however, that inclusion of this would resolve the above discrepancy in the phases.

IV SUMMARY AND DISCUSSION

The saturated state of a low frequency, coherent global mode has been studied in the Encore tokamak using probe techniques. The mode is found to have large fluctuations in density, electron temperature, space potential and magnetic field. The poloidal and toroidal mode numbers (m=2, n=1), as well as the radial structure of the fluctuations have been measured. The temperature fluctuations are found to be out of phase with the density fluctuations, consistent with expectations for a radiation dominated discharge. The space potential fluctuations are found to lead the density fluctuations by $\approx 45°$, indicating that the mode is transporting plasma radially inward.

The equilibrium plasma characteristics were also determined with probe measurements. Magnetic probes were used to determine the radial profile of the poloidal magnetic field, from which the rotational transform and current density profiles could be deduced. A Langmuir probe was used to measure radial profiles of the density, electron temperature and space potential. The space potential was nearly constant in the central region of the plasma, indicating that there was almost no $\mathbf{E}\times\mathbf{B}$ rotation of the plasma, i.e., the observed frequency of the mode was not Doppler shifted.

The experimental measurements were compared with the predictions of a code developed for the purpose. The code is based on a linear, two-fluid theory of the coupling of drift and shear-Alfven modes. Of the two shear-Alfven solutions and the drift branch solution, it was found that the drift wave solution best fit the observed frequency of the mode and the relative amplitudes of the density, space potential and magnetic fluctuations. The shear-Alfven solutions had much larger magnetic fluctuations for a given level of density fluctuations. The identification of the mode as a finite β_T modified drift wave means that the mode is more closely related to the higher frequency, turbulent fluctuations

observed on larger machines, rather than the lower frequency coherent Mirnov oscillations.

The Mirnov oscillations observed on larger tokamaks have many features in common with the finite beta modified drift wave observed in Encore, but the Mirnov oscillations are not likely to be drift waves. In larger tokamaks with hot, lighter ions, the ion thermal velocity becomes comparable to the parallel phase velocity of the mode a short distance from the rational surface. This would lead to ion Landau damping of the mode. Further, estimates of the ratio of magnetic to density fluctuations for larger machines, using Eq. (3.48), show that the magnetic fluctuation level would be too small by several orders of magnitude to explain the Mirnov oscillations. Using $T_e = 1\,\mathrm{keV}$, $B_T = 30\,\mathrm{kG}$, $n = 2\times10^{13}\,\mathrm{cm}^{-3}$ and $r = 40\mathrm{cm}$,

$$\frac{\tilde{B}}{B} \approx 3\cdot10^{-7}\,\frac{e\tilde{\Phi}}{T} \quad .$$

A similar calculation for the Encore tokamak would give

$$\frac{\tilde{B}}{B} \approx 10^{-2}\,\frac{e\tilde{\Phi}}{T} \quad .$$

Thus the large magnetic fluctuations associated with this drift wave are due in part to the relatively large ratio of ω/ω_{ci} and to a moderate plasma $\beta_T \approx .01$.

APPENDIX A: Numerical Integration

1 Introduction

This appendix describes the code CHARON which numerically solves Eqs. (3.29), (3.31), and (3.33) to find the eigenvalues and eigenfunctions of the density, space and vector potential fluctuations for electromagnetic drift and shear Alfven modes. CHARON is a shooting code which iteratively solves the differential Eqs. (3.29) and (3.31), and then calculates the density fluctuations using Eq. (3.33).

2 Equilibrium

Plasma discharges are characterized by the radial profiles of the density, electron temperature and safety factor, $q(r)$. In Encore it is found that the conductivity temperature and that determined from Langmuir probe measurements are different. It is found that the results of the theoretical calculations are not particularly sensitive to the temperature profile, and thus for simplicity the code uses a temperature profile calculated from the current profile, assuming Spitzer resistivity and a constant Z_{eff}. With the assumption that $\beta_T \ll 1$, which in turn implies poloidal symmetry, the poloidal field and plasma current density $J(r)$ can be calculated from $q(r)$. The code uses multiparameter analytical expressions to fit the density and $q(r)$ profiles. The $q(r)$ profile is fit to a standard function[24]:

$$q(r) = q_o \left(1 + \left(\frac{r}{r_1}\right)^{2\lambda}\right)^{\frac{1}{\lambda}} \qquad (A.1)$$

Thus the current profile is parametrized by q_o, r_1 and λ. The analytical expression for the density profile is somewhat more complex to allow greater flexibility in matching the complicated density profiles observed experimentally. The

function is:

$$n(r) = n_0 f_1(r) f_2(r) \exp\left[-(\frac{r}{r_0})^2\right] \tag{A.2a}$$

where $f_1(r)$ is a function that allows broader or narrower profiles than Gaussian:

$$f_1(r) = 1 + a_1(\frac{r}{r_1})^2 \exp\left[-(\frac{r}{r_1})^2\right] \tag{A.2b}$$

and $f_2(r)$ allows the introduction of hollow density profiles:

$$f_2(r) = \frac{(1 - (\frac{r}{r_2})^2) + \delta_1}{(1 - (\frac{r}{r_2})^2) + \delta_2} \tag{A.2c}$$

3. Numerical Integration

As there are two complex fields to be integrated, there will be two complex (or four real) eigenvalues in the problem. An attempt to solve both complex equations simultaneously proved awkward and slow. Instead, an iterative-perturbative approach was used. In this method, one of the complex fields ($\tilde{\Phi}$ or $\tilde{A}$) was treated as a perturbation, initially set equal to zero. The zero order solution was found, and the second equation was used to calculate the perturbation field. This field was then used in the initial equation to find the next order correction to the dominant field. This procedure was repeated until the eigenfunctions and eigenvalues converged to a stable solution. It was found that solving Eq. (3.31) for $\tilde{\Phi}$ first led to the drift solution, indeed the first solution of Eq. (3.31) with $\tilde{A} = 0$ would give the electrostatic drift wave solution. Solving Eq. (3.29) for $\tilde{A}$ would give one of the two shear-Alfven mode solutions, depending on the initial guess for the eigenvalues.

The equations were solved with a shooting code, using a standard numerical integration routine[25]. In this approach, an initial set of eigenvalues is chosen, the equations are integrated from the first to the second boundary, and the value of the field is compared to the specified boundary conditions. The eigenvalues are changed slightly, and the equations integrated again. For two eigenvalues, integration of the equations three times will yield sufficient information to make a linear extrapolation to the eigenvalues necessary to satisfy the chosen boundary conditions. This extrapolation gives only approximate eigenvalues, and the procedure must repeated until the eigenvalues give what has previously been decided as an adequate match to the boundary conditions. The code was run on an LSI-11/23 mini-computer. The typical running time to find the eigenvalues and functions for one mode for a specific set of plasma parameters was 30 minutes.

APPENDIX B: Probes

1. Langmuir Probes

The theory for Langmuir probes in unmagnetized plasmas[26,27] with cold ions predicts an I-V characteristic of the following form:

$$I_p(V) = I_s^i - I_s^e \exp\left[\frac{V_p - V_s}{T_e}\right] \qquad V_p \le V_s \tag{B.1}$$

where the ion saturation current and the electron saturation current are given by the following formulas:

$$I_s^i = e\, n_e\, c_s\, A \tag{B.2a}$$

$$I_s^e = e\, n_e\, v_{T_e}\, A\, (2\pi)^{-\frac{1}{2}} \tag{B.2b}$$

Here $c_s = (\frac{T_e}{m_i})^{\frac{1}{2}}$ and $v_{T_e} = (\frac{T_e}{m_e})^{\frac{1}{2}}$, and A is the effective collection area of the probe, equal to the area of the probe if $\lambda_{de} \ll r_{probe}$.

Equation (B.1) assumes that for probe bias voltages, V_p, less than the space potential, V_s, all ions incident on the probe are collected, and that the electron density at the surface of the probe obeys obeys the Boltzmann relation:

$$n = n_0 \exp\left[\frac{V_p - V_s}{T_e}\right] \tag{B.3}$$

As the ions are cold, the random ion current density will be zero, thus for Laplace's equation to be satisfied within the probe sheath region it is necessary that the ions be accelerated to $v_i \approx c_s$ before entering the probe sheath. The ions are accelerated in the 'pre-sheath', a region of slowly changing plasma potential extending far into the plasma.

Biasing the probe very negative will result in the collection of virtually no electrons, and thus the ion saturation current will be measured. The electron temperature and space potential are then determined by fitting the probe I-V

characteristic to Eq. (B.1) recast as:

$$V_p - V_s = T_e \ln\left[\frac{I_s^i - I_p(V)}{I_s^e}\right] \tag{B.4}$$

The potential at which the probe draws no current is called the floating potential, V_f. This potential is, from Eq. (B.4):

$$V_f - V_s = T_e \ln\left[\frac{I_s^i}{I_s^e}\right]$$

or:

$$V_s - V_f = \frac{1}{2} T_e \ln\left[\frac{m_i}{2\pi m_e}\right] \tag{B.5}$$

If the electron temperature is constant, then measurement of the fluctuations in the floating potential is equivalent to measurements of fluctuations in the space potential. Likewise, measurement of the ion saturation current will give a relative measurement of the density.

In the presence of strong magnetic fields, such that the particle Larmor orbit size approaches the size of the probe, Eq. (B.1) is modified because the particles can not move easily in directions perpendicular to the field. Thus, if the Larmor orbit size is smaller than the probe dimension, the effective area of the probe becomes twice the projected area on the plane perpendicular to the magnetic field. For cylindrical probes, this results in a reduction of the probe area by a factor of $\frac{2}{\pi}$. If the probe is collecting considerable current, as it will in the electron saturation regime, it may also deplete the plasma density on the flux tube in the region near the probe, as particles are inhibited from crossing field lines. A theory including this effect has been derived by Sanmartin[28], who shows that the electron component of the probe current is modified from that in Eq. (B.1) to:

$$I_e(V) \approx -I_s^e \exp\left(\frac{V_p - V_s}{T_e}\right)\left[1 - \varepsilon \exp\left(\frac{V_p - V_s}{T_e}\right)\right] \tag{B.6}$$

where

$$\varepsilon = \delta(Z_i)\,\frac{r_p}{r_{Le}} \tag{B.7}$$

and $\delta(Z_i)$ is a factor equal to 0.24 for $Z_i = 1$ and 0.18 for $Z_i = \infty$.

The ratio of the ion to electron saturation currents, as measured experimentally, is about 60; Eqs. (B.2a) and (B.2b) predict a ratio of 110. For this data, $r_{Li} \approx 10\,r_p$, $r_{Le} \approx 2\,r_p$ and $\lambda_{de} \approx .1\,r_p$ where $r_{Li,e}$ are the Larmor radii and the ions are assumed to be at room temperature, (.025 eV). As $r_{Li} \gg r_p$, the ion current will not be affected by the magnetic field, but the electron current will be reduced by ≈40% by density depletion,($\varepsilon \approx 0.4$), and by up to another 40% through geometrical effects. These predictions reduce the electron to ion saturation current ratio to between 40 and 70, consistent with the observed saturation current ratio of approximately 60.

The data were analyzed assuming no modification of the I-V characteristic due to the presence of a magnetic field. This is consistent with Eq. (B.6) as the I-V characteristic was measured only to voltages approximately (1–2) T_e below the space potential and the corrections to the electron current would be less than 6% due to density depletion. To test the sensitivity of the results to shadowing, the effective probe area for the electron current was changed by a factor of two, there was no qualitative change in the determination of the space potential. The self consistency of this approach was further tested by comparison of the calculated floating potential of the probe, based on the I-V and the ion saturation current, to that measured directly; they were found to be in good agreement.

Figure 12(a) shows a typical Langmuir probe. The metal wire is made of tungsten, chosen for resistance to sputtering. The sheath is alumina. The bare tip of the probe is 1 cm long and the probe diameter is .08 cm. The probe is sufficiently long so that it can be inserted past the center of the plasma.

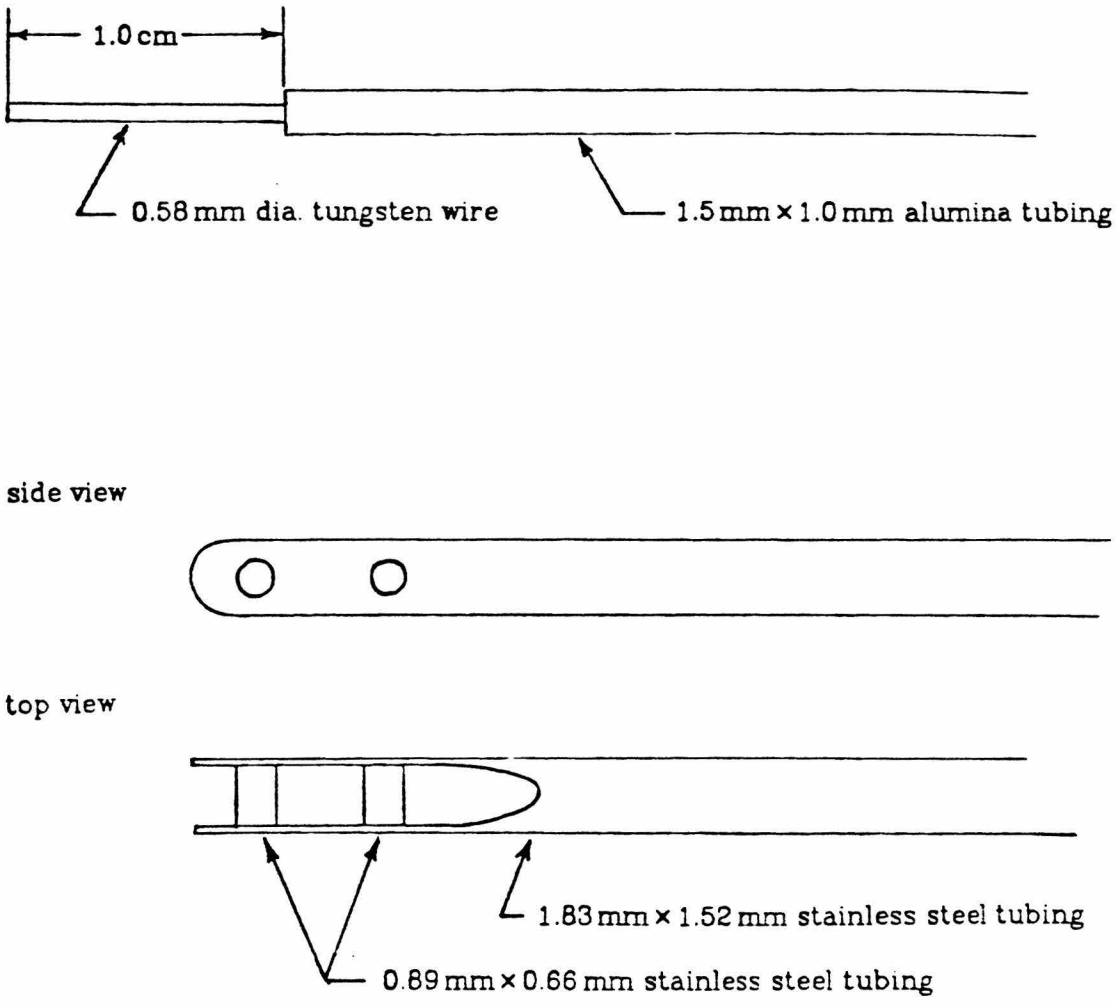

Figure 12. Details of the (a) Langmuir probe and (b) magnetic probe construction. The Langmuir probe was typically constructed of ≈ 0.6 mm tungsten wire with a 1.5 mm × 1.0 mm alumina insulating sheath. The length of the bare tip was 1.0 cm. The magnetic probe coils were wound on the coil form as shown in Fig. 12(b). Typically 80 turns of #44 magnet wire were wound on the form. The coil was center tapped, with the center tap connected to the coil form, which was in turn grounded (through the signal cable sheild) at the integrator. The coil assembly was inserted in a 6.0 × 3.0 mm closed alumina tube. Air was blown through the s.s. tube to cool the coil.

2. Magnetic Probes

Figure 12(b) shows the details of the construction of the magnetic probes. The magnetic probes consisted of multi-turn loops of wire wound on coil forms mounted at the end of thin wall, stainless steel tubing. Air was blown through the tubing to keep the probe coils cool. The coils were typically 80 to 100 turns of #44 (2 mil) magnet wire. The coils were center tapped, with the center tap connected to the return cable shield. The return cable shield, was in turn, grounded only at the integrator box, to minimize the effect of ground loops.

To minimize the effects of electrostatic pick-up, the coils were terminated in 20 ohms at the integrator input. The signals were integrated with analog integrators built using lf356 fet op-amps. The integrator used high quality, 10^{-8} F polystyrene capacitors and a 1.0 kΩ input resistor and was followed by an amplifier with a gain of ten. The integrator response could then be characterized as:

$$V_{out}(t) = 10^6 \sec^{-1} \int_0^t V_{in}(t')\,dt' \qquad \text{(B.8)}$$

The integrator drift could be nulled out to less than 1 mv/ms, giving a random offset to the data of 0.2 G.

The probes and integrators were calibrated with a Helmholtz coil, pulsed with a square wave from a transistor switch. The magnetic field in the Helmholtz coil was approximately 4.5 gauss. The integrator-coil system typically had sensitivities of 30 to 40 mv/G, adequate for the measurement of the 30 Gauss poloidal field with fluctuation levels of 0.5 to 1.0 gauss. The calibration was done with an oscilloscope, and thus the accuracy of the calibration was ≈ 5%.

APPENDIX C

1 Introduction

1. Discharges where $q(0) \approx 1$

In discharges where the central q of the plasma was of order one, evidence of coupling of poloidal modes by the toroidal geometry was found. In these discharges the electrostatic fluctuations were dominantly m=1, whereas the magnetic fluctuations were dominantly m=2. The frequency of the magnetic and density fluctuations was the same and the fluctuations maintained a constant phase relation from shot to shot. It is readily shown that toroidal effects can couple modes with adjacent poloidal mode numbers, i.e.; m to $m \pm 1$, but approximate theoretical models predicted much stronger coupling than was observed. More complete models were prohibitively complex, so this theoretical effort was abandoned.

In these discharges, the magnetic fluctuations had a mode rational surface at roughly .8 of the plasma minor radius. The fluctuations could then create magnetic islands, unlike the modes with $q(0) \approx 2$ described previously. From the experimental data, making assumptions about symmetry, the helical flux function, defined as:

$$F_H = 2\pi R_o \int_0^r B_{pol}(r') - \frac{nr'}{mR_o} B_T \, dr'$$

could be calculated and contours of a cross-section of the magnetic flux surfaces could be plotted (see Fig. 13). These surfaces show the size and structure of the magnetic islands. Similar measurements have been attempted with heavy ion beam probes on the ST tokamak[29] and with soft x-ray imaging techniques on PLT[30]. Robinson and McGuire made magnetic probe measurements on the

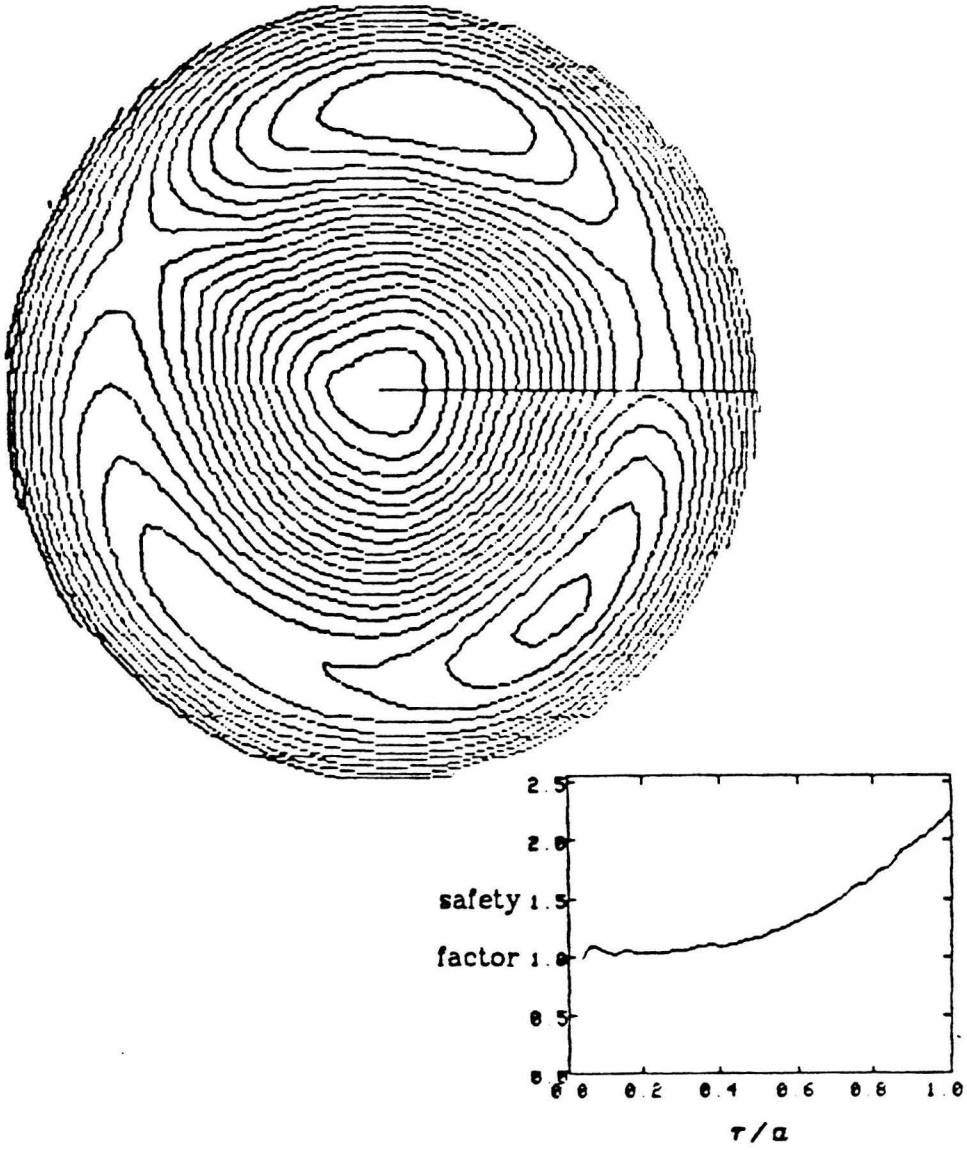

Figure 13. Contour plot of the helical flux function. As in Fig. 5, the poloidal angle is really the time axis. In this case, no effort was made to scale the time axis such that 360° corresponded to two periods of the oscillation.

Tosca tokamak[31], but in that case they were not able to insert the probes to the center of the machine.

2. Discharges where $q(0) > 2$

If the toroidal field were raised, keeping the plasma current constant, the plasma density and current density profiles would become flat in the center of the discharge, having strong gradients only near the edge of the machine. In these discharges, it was observed that the electromagnetic modes would become localized to the region of strong gradients. The transition from the low q to high q discharges could be done continuously; the modes were observed to change continuously from the global modes observed in the low q discharges to the radially localized modes of the higher q discharges.

3. Discharges where $q_o < 1$

An unusual regime for tokamak operation has been observed in the Encore tokamak. The normal limit for the stable operation of tokamak discharges is with $q(0) \approx 1$. In Fig. 14 are profiles of $q(r)$, and $\delta B_{T(r)}$ where $q(a) < 1$. In this regime, the low frequency, coherent oscillations present in discharges with higher q are absent. There is a relatively low level of higher frequency turbulent density and magnetic fluctuations, but in other respects the plasma is quiesant. The current, density and temperature profiles are not significantly different from those for discharges above $q(0) = 1$. The transition into and out of this state is abrupt, it has not been possible to operate with a $q = 1$ surface inside the plasma. A similar regime has recently been observed on the Wisconsin tokapole[32].

The radial profile of the changes in the toroidal field have been measured,

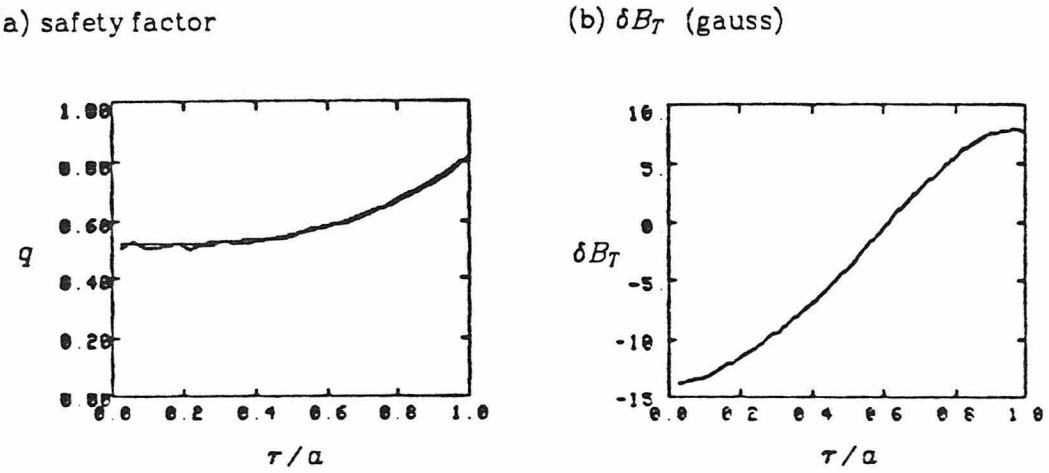

Figure 14. Radial profiles of the (a) safety factor and (b) change in toroidal field. These data were taken in a low q, strongly paramagnetic plasma. The safety factor has been fit to Eq. (A.1) with the parameters: $q_o = 0.52$, $r_1 = 0.96$ and $\lambda = 1.74$. The change in the toroidal field, δB_T, is due to a combination of the plasma paramagnetism from the poloidal component of the force free ohmic current, the diamagnetism from the gradient in the plasma β_T, and the flux conserving vacuum chamber walls. The 'dc' toroidal field for these data was -110 gauss.

showing the onset of flux reversal as is believed to exist in reverse field pinches. In this case the aluminum vacuum chamber, being very conductive, acts as a flux conserver. As the magnetic field lines become more twisted as the rotational transform increases, the plasma becomes more paramagnetic. To conserve the total toroidal flux, currents flow in the vacuum chamber walls opposite to the current in the toroidal field coils. Thus the toroidal field is increased in the machine center and decreased at the walls. The dc toroidal field for this discharge is -110 gauss, so the net change in the toroidal field at the center is $\approx 15\%$ and at the wall $\approx -7\%$.

LIST OF SYMBOLS

a	vacuum chamber minor radius
$\tilde{A}$	fluctuating component of the parallel vector potential
b	$k_\perp^2 \rho_s^2$
$\hat{b}$	unit vector parallel to the magnetic field
$\mathbf{B}$	magnetic field
c	speed of light in vacuum
c_s	ion sound speed
$D_\parallel$	classical parallel diffusion coefficient
e	magnitude of electron charge
$\mathbf{E}$	electric field
$\mathbf{J}_\parallel$	parallel component of the plasma current
$\tilde{\mathbf{J}}_\parallel$	fluctuating component of $\mathbf{J}_\parallel$
$\mathbf{J}_D$	electron diamagnetic current
$\mathbf{J}_{OH}$	force free ohmic heating current
$\mathbf{J}_o$	total equilibrium plasma current
$k_\parallel$	parallel wavenumber
n	plasma density
$\tilde{n}$	fluctuating component of the plasma density
m	poloidal mode number
m_e	electron mass
m_i	ion mass
P	plasma pressure (nT)
$\hat{r}$	radial unit vector
R	vacuum chamber major radius
T	electron temperature
$\tilde{T}$	fluctuating component of the electron temperature

$\mathbf{v}_{e,i}$	ion and electron fluid velocities
$\mathbf{v}_i$	ion velocity
V_A	Alfven velocity
V_l	one turn loop voltage
$x_j{}^m$	j'th zero of the m'th Bessel function
$\hat{z}$	axial unit vector
Z_{eff}	average ion charge state
α	$\equiv \gamma - \sigma(1-\gamma)$
β_T	ratio of plasma to magnetic pressure
γ	constant relating $\tilde{n}$ and $\tilde{T}$
$\tilde{\Gamma}_e$	fluctuating electron flux
$\tilde{\Gamma}_i$	fluctuating ion flux
η_s	Spitzer resistivity
$\hat{\theta}$	azimuthal (poloidal) unit vector
κ_o	(see page 26)
λ_d	Debye sheilding length
ν_{ei}	electron-ion collision frequency
ν_{ie}	ion-electron collision frequency
ρ_s	c_s / ω_{ci}
σ	coefficient of the thermal force
$\sigma(\tau)$	semi-hydrodynamic parallel electrical conductivity
$\tilde{\Phi}$	fluctuating component of the space potential
$\tilde{\Psi}$	non-Boltzmann electron response
ω	complex mode frequency
ω_{ci}	ion cyclotron frequency
ω_{*p}	electron diamagnetic frequency
ω_{*n}	density gradient electron diamagnetic frequency

ω_J characteristic current gradient frequency

$\Omega_{1,2}$ characteristic dimensionless drift wave frequencies

BIBLIOGRAPHY

[1]P. C. Liewer (manuscript in preparation).

[2]D. A. Monticello and R.B. White, Phys. Fluids 23, 366 (1980).

[3]J. F. Drake and Robert Kleva, Phys. Fluids 24, 1499 (1981).

[4]N. T. Gladd, J. F. Drake, C. L. Chang, and C. S. Liu, Phys. Fluids 23, 1182 (1982).

[5]K. T. Tsang, J. C. Whitson, and Julius Smith, Phys. Fluids 22, 1689 (1979).

[6]Swadesh M. Majahan, R. D. Hazeltine, H. R. Strauss, and David W. Ross, Phys. Fluids 22, 2147 (1979).

[7]George Schmidt, *Physics of High Temperature Plasmas 2nd Ed.*, (Academic Press, Inc., New York, 1979) p. 354.

[8]T. J. M. Boyd and J. J. Sanderson, *Plasma Dynamics*, (Barnes & Noble, Inc., New York, 1969) p. 83.

[9]Yasushi Nishida and Kazushige Ishii, Phys. Rev. Lett. 33, 352 (1974).

[10]J. T. Tang and N. C. Luhmann,Jr., Phys. Fluids 19, 1935 (1976).

[11]D. E. Post, R. V. Jensen, C. B. Tarter, W. H. Grasberger, and W. A. Lokke, Princeton Plasma Physics Laboratory Report No. 1352 (1977).

[12]Glenn Bateman, *MHD Instabilities*, (MIT Press, 1978) p. 129.

[13]A. B. Hassam, Phys. Fluids 23, 38 (1980).

[14]Lyman Spitzer, Jr., and Richard Harm, Physical Review 89, 977 (1953).

[15]V. D. Shavranov, in *Reviews of Plasma Physics*, edited by M. A. Leontovich (Consultants Bureau, New York, 1966), Vol. 2, p. 103.

[16]B. B. Kadomtsev and O. P. Pogutse, in *Reviews of Plasma Physics*, edited by M. A. Leontovich (Consultants Bureau, New York, 1966), Vol. 5, p.284.

[17]H. W. Hendel, T. K. Chu, and P. A. Politzer, Phys. Fluids 11, 2426 (1968).

[18]N. T. Gladd and C. S. Liu, Phys. Fluids 22, 1289 (1979).

[19]R. F. Ellis and R. W. Motley, Phys. Fluids 17, 582 (1974).

[20]S. I. Braginski, in *Reviews of Plasma Physics*, edited by M. A. Leontovich (Consultants Bureau, New York, 1965), Vol. 1, p. 214.

[21]H. P. Furth, P. H. Rutherford, and H. Selberg, Phys. Fluids 16, 1054 (1973).

[22]J. F. Drake and Y. C. Lee, Phys. Fluids 20, 1341 (1977).

[23]B. B. Kadomtsev, *Plasma Turbulence*,
(Academic Press, New York, 1965), p. 82,83.

[24]B. Carreras, B. V. Waddell, H. R. Hicks, Nucl. Fusion 19, 1423 (1979).

[25]Scientific Subroutines Reference Manual AA-1101B-TC,
(Digital Equipment Corporation, Maynard, Massachusetts, 1978) p. 3-33.

[26]F. F. Chen in *Plasma Diagnostic Techniques*, R. H. Huddlestone
and S. L. Leonard, Eds. (Academic Press Inc., New York, 1965), p. 113.

[27]J. Laframboise, Institute for Aerospace Studies, University of
Toronto UTIAS Report No. 100, 1966.

[28]Juan R. Sanmartin, Phys. Fluids 13, 103 (1970).

[29]J. C. Hosea, F. C. Jobes, R. L. Hickok, and A. N. Dellis,
Phys. Rev. Lett. 30, 839 (1973).

[30]N.R. Sauthoff, S. Von Goeller, W. Stodiek, Nucl. Fusion 18, 1445 (1978).

[31]D. C. Robinson, and K. McGuire, Nucl. Fusion 19, 115 (1979).

[32]T. H. Osborne, R. N. Dexter and S. C. Prager,
Bull. Am. Phys. Soc. Vol. 27, 972 (1982).